High Productivity Milling of Calcium Polyphosphate

by

Theodoros Vasilopoulos

A thesis
presented to the University of Waterloo
in fulfillment of the
thesis requirement for the degree of
Master of Applied Science
in
Mechanical Engineering

Waterloo, Ontario, Canada, 2012

Author's Declaration

I hereby declare that I am the sole author of this thesis. This is a true copy of the thesis, including any required final revisions, as accepted by my examiners. I understand that my thesis may be made electronically available to the public.

Abstract

The main objective of this thesis is to further reduce the machining cycle time for producing Calcium Polyphosphate (CPP) implant constructs. To achieve this, the impregnation of the CPP lattice with various polymers is investigated, with the aim of improving the toughness of the material. By applying Taguchi's orthogonal array method it was determined that CPP infiltrated with an ionic bonding polymer produces the best material for generating high quality machined surfaces and features. While there is some loss in surface porosity, in comparison to cutting uninfiltrated CPP, the porosity loss was deemed acceptable for the clinical purpose of the implant, and in many cases, would be trimmed off during a consecutive finish machining operation.

The 2 fluted 4 mm diameter flat end mill at a cutting speed of 30 m/min and ¾ immersion up-milling, 0.1 mm chip load and 3 mm depth of cut were determined to be highly suitable for achieving both high productivity as well as excellent surface integrity. These conditions produced a material removal rate of 4,302 mm^3/min, which was 14 times higher than the material removal rate achieved in machining pure CPP in earlier studies. The constructed machining model was highly successful in predicting the cutting forces, and therefore can be used in process planning and optimization in the production of tissue engineered implant constructs out of CPP.

The Finite Element analyses predicted that the implant would not chip or break during the roughing operation, as validated experimentally. This allowed the roughing cycle time to be reduced from 159 min to 19 min, effectively achieving a productivity improvement of 8 times over the earlier work done in this area.

Acknowledgements

I would like to thank my parents, siblings and my fiancé who helped me through the good and tough times while completing my thesis. Also, a special thanks to my supervisors and committee members for reviewing my thesis and providing me with positive feedback and the proper corrections to obtain a well-organized thesis.

Table of Contents

List of Figures

List of Tables

CHAPTER 1
Introduction

1.1 Synopsis

This thesis targets improvement of the machining productivity of Calcium Polyphosphate (CPP), which is a porous biodegradable ceramic that is currently being investigated as a substrate material for tissue engineered biomedical implants. Earlier studies conducted at the University of Toronto and Mount Sinai Hospital [8] have revealed that CPP has the potential of being an excellent bone substitute due to the following reasons:

- The compressive and tensile strength of CPP are significantly higher (~38 MPA and 9 MPa, respectively) compared to that of Hydroxyapatite (~28 MPa and 3 MPa, respectively) [31], where Hydroxyapatite is one of most commonly used biodegradable implant materials.
- The porous structure of CPP allows excellent support for in-vivo cell seeding, thus enabling laboratory-grown cartilage to be formed on the implant surface prior to implantation, as illustrated in Figure 1.1.
- The porosity of the CPP also facilitates revascurilazation of blood vessels, which accelerates bone healing and in-growth, as opposed to bone-loss which is the common problem encountered in most bone-to-metal contact implants.

- As the original bone heals and grows into the volumetric shape of the implant, CPP disintegrates in the host's body leaving behind only Calcium ions and phosphate compounds, which can be absorbed into, and removed by the host organism without encountering any biocompatibility issues.

Therefore, the utilization of CPP as a tissue engineering implant material has been under heavy investigation throughout the recent years, by researchers from the University of Toronto and Mount Sinai Hospital [8][12][13][14].

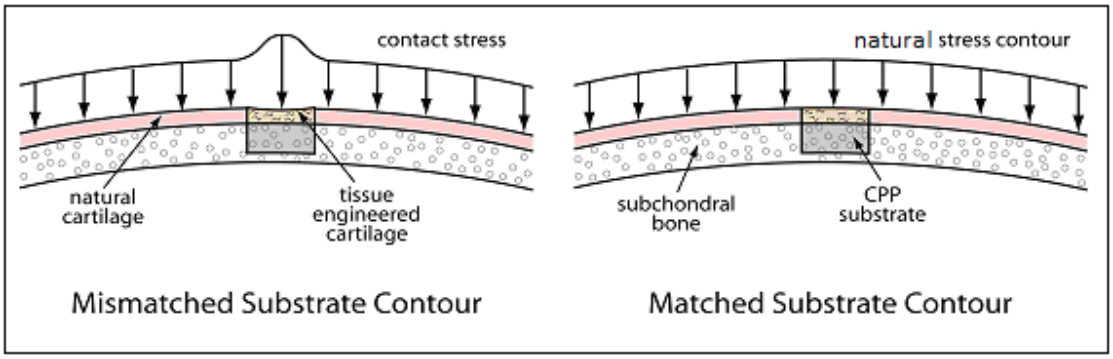

Figure 1-1: Method of in vivo and in vitro grown tissue-engineered cartilage [15].

In tissue engineered implant design, in addition to achieving good mechanical compatibility between the substrate material and the original tissue/bone region in terms of strength, elasticity, and fracture toughness, it is also vital that the volumetric shape of the implant display a certain level of compliance with the geometry of its surrounding features, in order to distribute mechanical loads evenly without leading to unnecessary stress concentrations.

In 2005, to assess the performance of tissue engineered CPP implants under realistic application and loading conditions, it was found necessary to shape various portions of CPP implants according to actual anatomical features. Hence, it became necessary to develop new methods of shaping such implants into complex geometries, which could not be achieved simply through the use of slip casting dies and moulds prior to sintering the implants according to a standard protocol [15]. Especially, for producing customized bone implants that are to be designed directly through the use of CT scan data from individual patients, it is imperative to have reliable, efficient, and accurate shaping techniques for CPP. Thus, collaboration was initiated between the University of Waterloo and the University of Toronto, where Waterloo

researchers (Prof. E. Toyserkani and Prof. K. Erkorkmaz) were charged with the task of investigating such manufacturing methods to impart complex 3D geometries onto CPP structures.

Prof. Toyserkani's group has focused on additive methods involving the use of solid freeform fabrication (SFF) to produce the implants very quickly and with minimal CPP powder loss [12][15]. Prof. Erkorkmaz' group, on the other hand, has investigated the use of machining techniques [15][16] that achieve high levels of accuracy and good surface porosity. Unfortunately, machining also causes a lot of sintered CPP material, which is expensive and labour intensive to manufacture, to be wasted. Other disadvantages of machining are the excessive manufacturing cycle time and the risk of destroying the implant due to cutting force overload or excessive vibrations, which can result in cracking and brittle breakage. It is obvious that both SFF and machining have distinctive advantages and drawbacks for shaping CPP, and perhaps could be used in a sequence where their strengths could be combined and weaknesses mitigated, such as producing near-net-shaped implants first as green parts using SFF, and after they are sintered, machining them to their final geometry, features, and dimensions with minimum powder loss and in machining time, using multi-axis machining.

This thesis targets furthering the CPP machining conditions that were achieved in [16], and reported in [8]. The methods applied in this thesis and the benefits obtained are applicable in both cases, where machining is used as a stand-alone operation to shape post-sintered CPP blanks from basic 3D shapes like prisms or cylinders, or it is used as a complementary operation post-sintering, after near-net-shape green substrates are first produced using solid freeform fabrication.

1.2 Earlier Machining Work for CPP

During the most recent study [16][8], a mechanistic cutting force model was developed for machining 70% density CPP with 45-150 um particle size using milling. The machining conditions comprising of cutting speed, tool/workpiece engagement conditions, cutting depth,

and chip load were selected by trial and error in order to yield the most favourable results in terms of surface porosity, geometric feature retention and machining productivity, though a limited number of preliminary experiments. It was determined that using up-milling in up to full immersion with 1-2 mm depth of cut, 50-150 mm/min cutting speed range, and 0.05 mm/tooth chip load, kept the resulting cutting force below 45 N and was able to produce acceptable results with open surface porosity and good geometric features without chipping. Ultimately, these findings were incorporated into planning the 5-axis machining operation for producing a tibial-plateu (lower knee joint) implant, which was designed by researchers led by Prof. R.M. Pilliar and Prof. R. Kandel from the University of Toronto and Mt. Sinai Hospital. The developed machining procedure is shown in Figure 1.3.

While the CPP implant, as seen in Figure 1.4, could be produced with high accuracy, good surface porosity and acceptable dimensional integrity, the total machining cycle time for all of the phases was nearly 5 hours (160 min for roughing, 70 for semi-finishing, and 60 for finishing). In a clinical application involving the custom manufacture of bone implants based on CT scans, such a long shaping duration may be unacceptable.

1.3 Aims and Contributions of this Thesis

The main objective of this thesis is to further reduce the machining cycle time for producing CPP implant constructs. To achieve this objective, the impregnation of the CPP lattice with various polymers is investigated, with the aim of improving the toughness of the material and therefore its resistance to cracking and chipping during elevated cutting speeds as well as aggressive chip loads and cutting depths. Post machining, the polymers would be burned off by heat-treating the implant, along with any hydrocarbons that could have contaminated the CPP during the machining or handling operation.

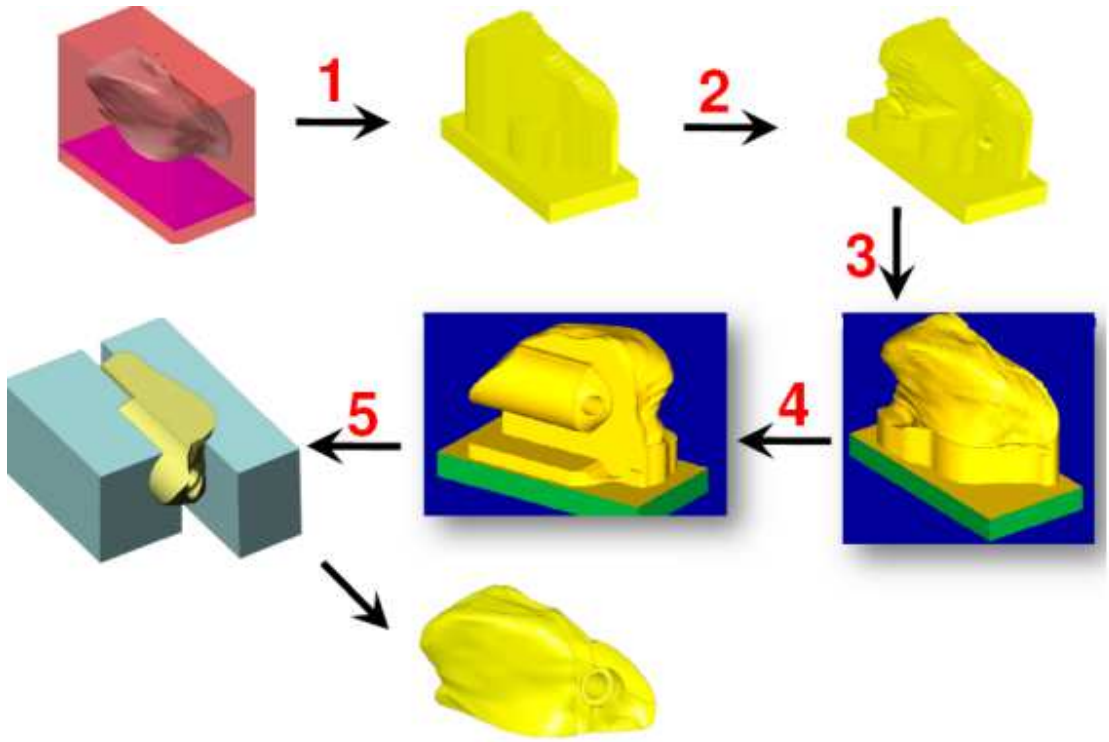

Figure 1-2: Developed implant machining steps in [16]: Figure 1: 1) 3-axis roughing, 2) 5-axis roughing, 3) 5-axis finishing, 4) Keel surfacing and hole drilling, 5) Flat surface machining inside a conformal wax clamp.

According to Figure 1.4, it is clear that the roughing cycle takes the largest amount of time in the scenario where the complete implant is shaped using solely machining. Therefore, the focus in this thesis has been to devise the design-of-experiment and use correlation techniques that would help identify the cutting conditions which would dramatically reduce the roughing time for the implant. These conditions have afterwards been adopted in the production of implants, which are currently being used in pre-clinical trials on sheep. The design-of-experiment was realized using the Taguchi Method. After identifying the important factors that influenced the CPP machining operation, initially a 9-experiment L_9 array, followed by a 4-experiment L_4 array, was executed. These experiments helped to determine the most suitable machining conditions that significantly reduced the roughing cycle time, and also yielded CPP substrates with

acceptable dimensional and surface quality. These studies were complimented with Finite Element (FE) analyses, which helped to determine toolpath planning configurations to reduce the stress loading on the workpiece. This meant that higher chip loads and cutting depths could be adopted, thereby also improving the machining productivity, without breaking the implant. The overall results of these studies have been incorporated into a 5-axis machining strategy, which has been validated experimentally.

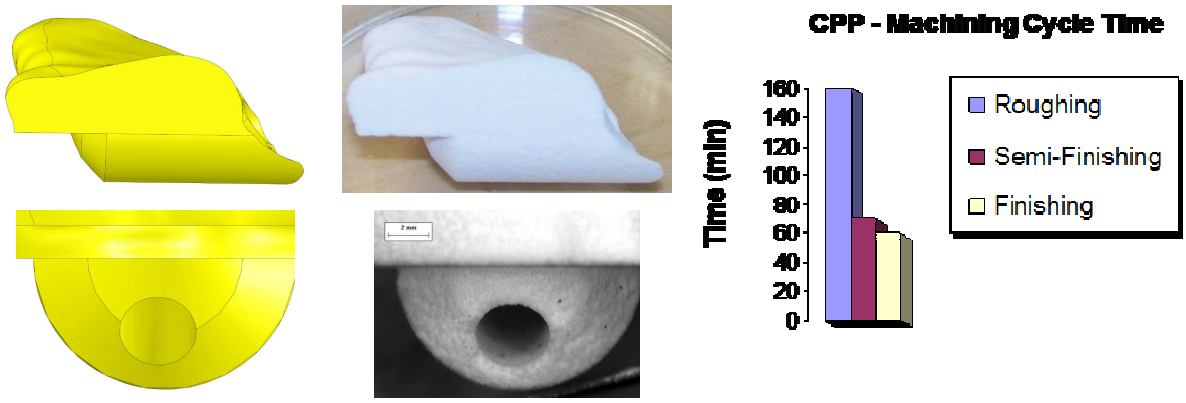

Figure 1-3: Machined implant and machining time break-down [8].

It is important to point out that while the main focus of this thesis was to minimize the cycle time for the roughing stage, the same design-of-experiment and Finite Element analysis could also have been applied to improve the machining conditions for semi-finishing and finishing stages, in the case where multi-axis machining is to be used following the sintering operation, after a near-net-shape implant is first produced using solid freeform fabrication.

Henceforth, the thesis is organized as follows: Chapter 2 presents a literature review, followed by the main design of experiment in Chapter 3, which has helped determine the most suitable CPP and polymer combination to be used in the remaining machining studies. Chapter 4 narrows down the search for the optimal machining conditions by investigating the influence of the chip load and depth of cut during the roughing process. Also, sample implants are produced by applying the findings obtained so far to 5-axis toolpath planning. It is shown that at least 140 minutes reduction in the roughing cycle time, and an overall 2 hours and 20 minutes reduction in the time required to produce one complete implant can be achieved, compared to the results that were reported in [16][8]. Also in Chapter 4, FE analyses are conducted for critical portions of the

machining operation, that help determine better configurations that reduce the stress loading on the CPP implant. As a result, the 5-axis machining toolpaths are revised to allow more aggressive machining conditions to be realized, thereby allowing a further 140 minutes reduction in the cycle time. These toolpaths are also validated experimentally. Finally, the conclusions for this thesis are presented in Chapter 5.

CHAPTER 2

Literature Review

Calcium Polyphosphate (CPP) material has been proposed as an alternative to metallic implants for use in fracture fixation applications [8]. The mechanical strength of the biodegradable fixation decreases with time and gradually transfers the load to the healing bone, thus reducing shielding stress that leads to osteoporosis [13]. The material is degraded and eliminated by excretion and resorption, so that the removal of the device by operation is not necessary. This reduces the cost of the treatment when compared to metallic implants.

CPP is also porous, which allows for chondrocytes to enter into the pores. Cartilage that forms in the region anchors the tissue to the CPP. With CPP being porous, bone grows into the pores, which is not filled by cartilage after implantation, which results in the implant being secured and fixed in place. This is why surface porosity is vital to cell growth.

2.1 Solid Freeform Fabrication (SFF) of Calcium Polyphosphate (CPP)

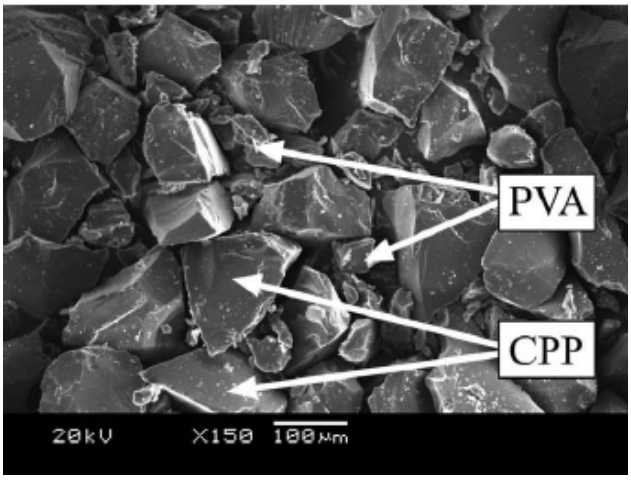

Figure 2-1. Scanning Electron Microscope (SEM) of PVA-CPP blend powder [12].

A method that is currently being investigated for manufacturing Calcium Polyphosphate shapes is Solid Freeform Fabrication (SFF). This techniques allows the fabrication of anatomically shaped porous components by building the geometry up in layers. SFF systems are considered to function in one of the three categories based on the original structure of the material they apply, which can be: liquid-based, solid-based, or powder-based.

This method of manufacturing has been investigated by Shanjani [12] in the Rapid Prototyping Laboratory of the University of Waterloo. CPP powder of 75–150 μm was mixed with polyvinyl alcohol (PVA) polymeric binder and was used in the SFF machine with appropriate settings for the powder mesh size, as shown in Figure 2-1. The PVA binder was then removed during an annealing process and the preformed shape was sintered. The few samples that were measured with a micro-CT scanner had 32% porosity. The average pore size was around 53 μm. To obtain these results, mercury porosimetry was used. The compressive strength of 6 mm cylinders was measured, using 10 samples, as 33.86 ± 6.33 MPa.

2.2 Machining of Porous Calcium Polyphosphate (CPP)

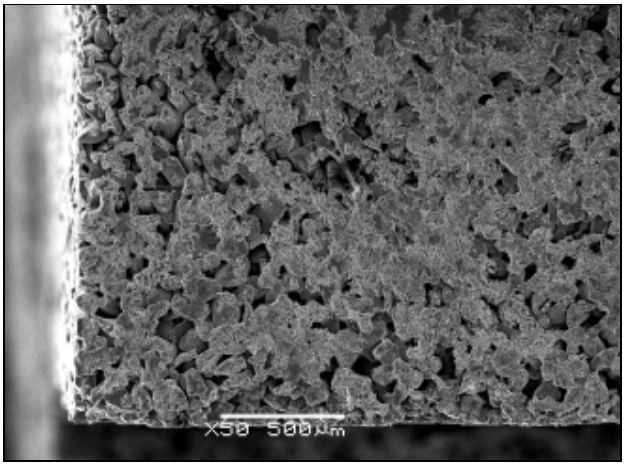

Figure 2-2. SEM image of a machined CPP specimen [8].

Another method of fabricating porous CPP shapes out of sintered pre-forms is machining. Machined porous CPP structures with 30 percent volume of interconnected pores and spaces between each network of pores that have 50-150 micron range were determined to be suitable for bone and cartilage ingrowth [22][23][24]. Based on the results of diametral compression testing [8], the compressive strength of 70% dense machined CPP was measured to be around 38 MPa.

Unfortunately, CPP is a brittle material which is difficult to machine. Overcoming this difficulty is the main objective of this thesis. It is also vital that the manufactured implant adequately mimics the geometry and stiffness characteristics of the original bone structure, in order to avoid unwanted stress concentrations that could damage the implant, deteriorate the cell adhesion and bone ingrowth characteristics, or damage the in-vitro grown cartilage layer. Figure 2-2 is a Scanning Electron Microscope (SEM) image of a machined CPP specimen taken from [8], which was produced by milling at a cutting speed of 50 mm/min and chip load of 0.0167 mm/tooth. It is clear that conservative these parameters are capable of producing accurate and clean edges, sharp corners, and a porous surface. However, these feeds and speeds which are conservative also results in excessive cycle times for producing implants; in the order of 6 hours per piece. One of the major aims in this thesis is to improve the machining productivity of CPP while retaining the feature and surface quality characteristics.

2.3 Infiltrating Porous CPP with Polycarbonate Resin

The disadvantage of porous CPP is its brittleness and poor fracture toughness, which results in low elastic deformation capability for load bearing applications. Biodegradable Interpenetrating Phase Composites (IPC) provide an ideal case for strength increase in porous CPP. They consist of two or more 3D continuous phases that interpenetrate with each other [25][26]. Polycarbonate diol (PCN) based divinyl oligomer, along with methacrylic acids (MA), can be produced to cross link polymer resins [21]. A ratio of PCN divinyl oligomer and MA of 1:20 has an interfacial shear strength of 6.71 MPa, which results an increase in strength when compared with the non-ionic resin, which achieves 1.5 MPa [21]. The polymer backbone of polycaprolactone consists of ester groups that hypothetically can only provide weak van der Waal's interactions with CPP. It was studied in [21] that the higher proportion of oligomeric polycarbonate and lower number of MA groups were assumed to have contributed to a decrease in the mechanical strength. Also, it seems that the increase in the amount of MA indicates a stronger interaction with the CPP fibers, which translates into higher bending strength and an increase in toughness.

In this thesis, one approach that will be investigated as a means of improving the machinability of CPP is to infiltrate the matrix with various resins that either form ionic bonds, or only achieve van der Waals interactions.

2.4 Conclusions

This chapter has provided a review of the current state-of-research being conducted for shaping CPP into functional implants. This includes SFF and machining. Earlier work has also indicated that polymer impregnation has the capacity to improve the strength of CPP. The impact of this idea on improving the machining quality and productivity will be investigated in this thesis.

CHAPTER 3

Identification and Optimization of the Most Significant Factors that Influence the Machining of CPP

3.1 Introduction

This chapter investigates the most significant factors that influence the machining process for sintered CPP, with the aim of optimizing these factors so that implants of acceptable quality can be produced by machining in the shortest cycle time.

Due to its versatility for producing complex freeform shapes, milling is chosen as the means of imparting the desired geometry onto prismatic CPP blanks. Hence, the chapter begins with a brief look at milling mechanics in Section 3.2. In Section 3.3, the manufacturing conditions believed or observed to influence the milling operation are identified for experimental investigation. While the choice of cutting tool and machining parameters plays a major role, the composition of the CPP blank is found to be just as important. One of the main contributions of this thesis is to investigate whether impregnating the CPP structure with certain polymers, as discussed in Section 3.3; helps improve the machinability of this material.

Due to the relatively high cost of manufacturing CPP blanks in small batches, the machinability of this material needs to be studied while consuming the minimum number of specimens. This has motivated the use of Taguchi's design-of-experiment methodology [3], which helps to configure the minimum number of experiments that need to be executed in order to reliably assess how different factors contribute to the machining outcome. An overview of

Taguchi's method is provided in Section 3.4, followed by its adaptation to the research problem at hand, in Section 3.5, according to the factors that are identified in Section 3.3.

Evaluation of the test results is realized in Section 3.6. The two responses considered to be the most relevant are machined surface integrity (for producing the desired geometric features without chipping the implant), and surface porosity (to ensure that the implants achieve their desired clinical function of cell seeding and bone regeneration). Both responses are measured visually by capturing optical and Scanning Electron Microscope (SEM) images, and evaluated using subjective and quantitative means. Parallel to visual observations and discussions, a statistical Analysis of Variance (ANOVA) is also conducted for both responses, in order to gauge the most significant factors that influence each response. Main results of these analyses are presented in Section 3.7, which indicate that polymer impregnation can indeed improve the productivity of the operation while retaining excellent surface integrity and acceptable porosity.

3.2 Cutting Mechanics of Milling

This section provides a brief review of the cutting mechanics for milling operation. Further details can be found in [1].

In milling, the cutter rotates and relative translational motion is realized between the workpiece and cutter, in order to achieve the desired material removal. Figure 3-1 provides an illustration of the two most commonly used configurations in milling, which are up- and down-milling; also referred to as conventional and climb cutting, respectively. By looking at Figure 3-2, the engagement of the rotating cutting edge with the workpiece can be analyzed in a generalized manner by considering instantaneous angle of the cutting edge (ϕ), which is measured from the y-axis that is orthogonal to both the feed direction (x-axis) and the axis of cutter rotation (z-axis). This edge will be removing material from the workpiece whenever ϕ is between the interval defined by the entry and exit angles, ϕ_{st} and ϕ_{ex} respectively.

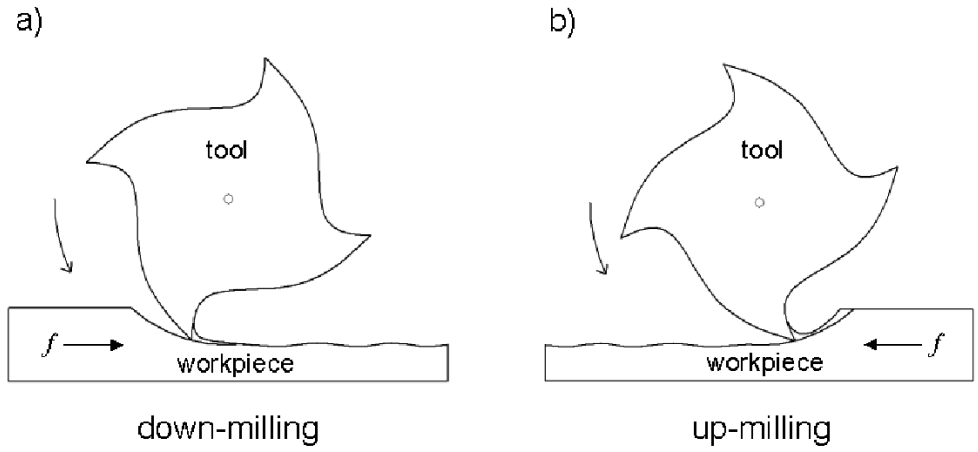

Figure 3-1: Down-milling and up-milling operations; 'f' designates the feed direction [17].

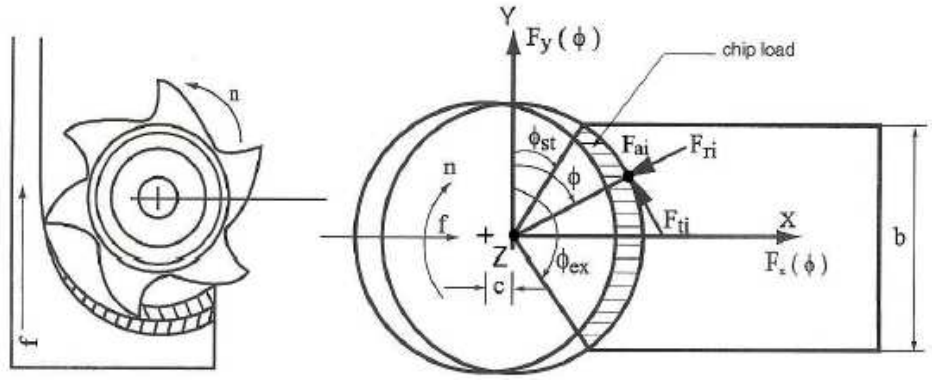

Figure 3-2: Geometry of an End Milling Process [1].

Each cutting edge on the endmill creates a periodic chip thickness that varies during the tooth passing cycle. The chip thickness generated can be approximated as [1],

$$h(\phi) = c \sin \phi \tag{3.1}$$

Above, c represents the amount of feed per tooth, or "chip load".

If the cutting edges on an end mill are helical, the instantaneous immersion angle of a point on the cutting edge "i" will be a function of the helix angle of the tool (β), the axial height (a) of this point from the tip of the cutter, and the pitch angle ϕ_p, which defines the angular clearance between consecutive cutting edges, as shown in Figure 3-3. For example, a uniform-pitch cutter with two flutes would have ϕ_p=180°.

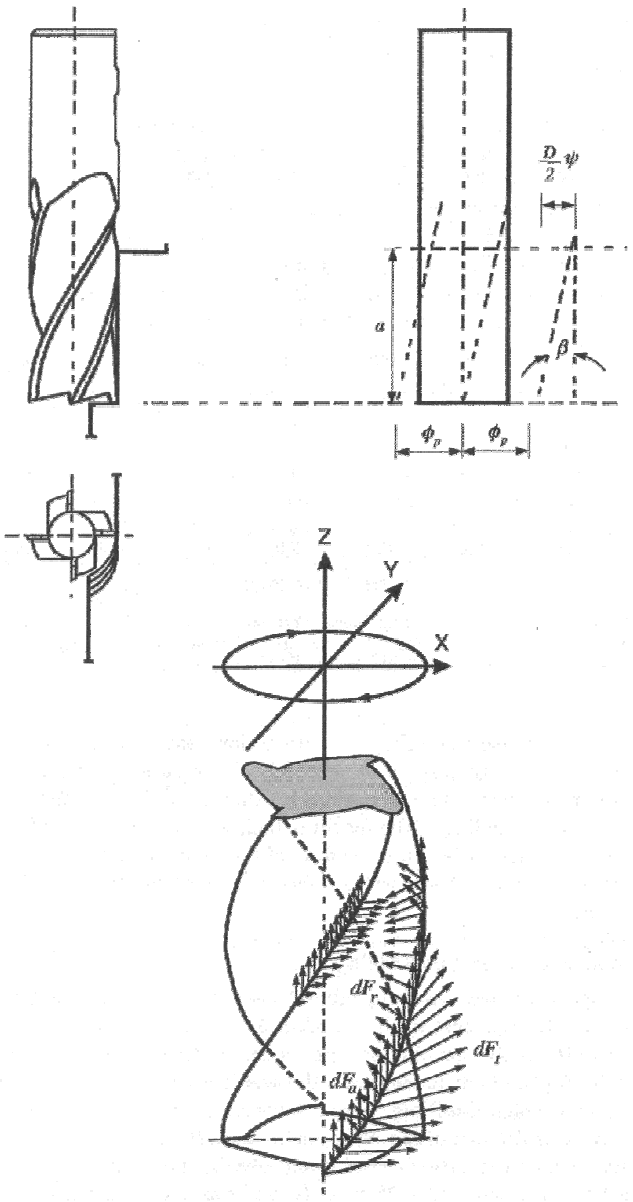

Figure 3-3: Geometry of Helical End Milling [1].

In this case, the instantaneous chip thickness generated by such a point on the cutting edge i would be expressed as,

$$h_i(a) = c\sin\phi_i \quad , \quad \text{where}: \quad \phi_i = \phi + i\phi_p - [(2\tan\beta)/D]a \tag{3.2}$$

Above, D is the diameter of the cutter and ϕ represents the rotation angle of the first cutting edge at the tip of the tool. By applying the Finite Element method, as illustrated in Figure 3-3, if this point is considered to generate a cutting force along an axial discretization length of dz; using the oblique cutting model [1], components of this force in the tangential, radial, and axial directions (dF_t, dF_r, and dF_a, respectively) with respect to the milling operation as illustrated in Figures 3-2 and 3-3, can be calculated as:

$$\begin{aligned} dF_{t,i}(\phi,a) &= [K_{tc}h_i(\phi_i(a)) + K_{te}]da \\ dF_{r,i}(\phi,a) &= [K_{rc}h_i(\phi_i(a)) + K_{re}]da \\ dF_{z,i}(\phi,a) &= [K_{ac}h_i(\phi_i(a)) + K_{ae}]da \end{aligned} \tag{3.3}$$

Above, K_{tc}, K_{fc}, and K_{ac} are the cutting force coefficients that determine how much force is generated per uncut chip area ($h_i \times da$) to achieve the required chip shearing mechanism for cutting. K_{te}, K_{re}, and K_{ae}, on the other hand, represent how much additional force is generated due to the chip rubbing along the rake face of the milling cutter. These coefficients will be identified experimentally when characterizing the CPP machining operation in Chapter 4. It is important to note that the incremental force components in Eq. (3.3) will be zero when a particular section of the flute is not engaged in the cut (i.e. if $\phi_{st} \le \phi_i \le \phi_{ex}$ does not hold, then $dF_{t,i} = 0$, $dF_{r,i} = 0$, and $dF_{a,i} = 0$).

Considering the geometry of milling in Figure 3-2, the differential force components can be projected to the x- (feed) y- (normal), and z- (axial) directions as:

$$\left.\begin{aligned} dF_{x,i}(\phi_i(a)) &= -dF_{t,i}\cos\phi_i(a) - dF_{r,i}\sin\phi_i(a) \\ dF_{y,i}(\phi_i(a)) &= +dF_{t,i}\sin\phi_i(a) - dF_{r,i}\cos\phi_i(a) \\ dF_{z,i}(\phi_i(a)) &= dF_{a,i} \end{aligned}\right\} \tag{3.4}$$

Hence, the total force in the x-, y-, and z-directions can be obtained by summing up the individual force contributions as:

$$F_x(\phi) = \sum_{k=0}^{L-1}\sum_{i=0}^{N-1} dF_{x,i}(\phi_i(k\cdot da)) \quad , \quad F_y(\phi) = \sum_{k=0}^{L-1}\sum_{i=0}^{N-1} dF_{y,i}(\phi_i(k\cdot da))$$
$$F_z(\phi) = \sum_{k=0}^{L-1}\sum_{i=0}^{N-1} dF_{x,i}(\phi_i(k\cdot da)) \tag{3.5}$$

Above, N is the total number of flutes and L is the total number of length-wise elements considered in the computation. The individual force components can be combined to obtain the resultant cutting force:

$$F(\phi) = \sqrt{F_x^2(\phi) + F_y^2(\phi) + F_z^2(\phi)} \tag{3.6}$$

According to this model, the average values of cutting forces can be predicted per Eq. (3.7), if the cutting coefficients, tool geometry, and engagement angles are known:

$$\overline{F}_x = \left\{ \frac{Nac}{8\pi}[K_{tc}\cos 2\phi - K_{rc}(2\phi - \sin 2\phi)] + \frac{Na}{2\pi}[-K_{te}\sin\phi + K_{re}\cos\phi] \right\}_{\phi_{st}}^{\phi_{ex}}$$
$$\overline{F}_y = \left\{ \frac{Nac}{8\pi}[K_{tc}(2\phi - \sin 2\phi) + K_{rc}\cos 2\phi] - \frac{Na}{2\pi}[+K_{te}\cos\phi + K_{re}\sin\phi] \right\}_{\phi_{st}}^{\phi_{ex}} \tag{3.7}$$
$$\overline{F}_z = \frac{Na}{2\pi}\left[-K_{ac}c\cos\phi + K_{ae}\phi\right]_{\phi_{st}}^{\phi_{ex}}$$

Equation (3.7) can also be used to estimate the cutting coefficients when there is experimental data available about the average cutting forces generated by a given material and tool pair.

In Chapter 4 of this thesis, a machining model for milling polymer infiltrated CPP will be established by identifying the cutting force coefficients for this material and validating the model with simulations. These tasks were realized using CutPro machining process simulation and analysis software, which applies the theory summarized in Eq. (3.1)-(3.7).

3.3 Factors that Influence the Machining of CPP

In planning a robust design-of-experiment, it is important to recognize the factors that influence the outcome. Then chip load, cutting speed, and depth of cut of the tool relative to the workpiece can all play an influential role on the machining productivity. These, as well as other factors believed to affect the machining process, are listed in the following along with particular design choices that will be made related to the machinability experiments, which will be conducted in the latter portion of this chapter.

1. Material

The brittle nature of porous CPP makes it quite difficult to machine at high productivity rates. While there is the possibility of obtaining different structures for CPP, the purpose of the current sintering protocol is to generate a porous material to fulfill the afore mentioned biomedical functions. However, one main hypothesis that is investigated in this thesis is whether infiltrating the CPP lattice with a polymer can help improve the ductility and chipping resistance of this material, in order to be able to withstand heavier machining cuts. Two kinds of polymers will be explored; one which does not form any ionic bond with CPP, and another one which does. Hence, the material factor will be investigated in 3 levels:

- **1a. Pure CPP (*70% density, 45-105 micron particle size*):** This will be the "control" material, corresponding to the same material used in earlier studies [8].

- **1b. CPP Infiltrated with a Non-Bonding Polymer:** After following the standard protocol for making a CPP block [18], the block was soaked inside a mixture of benzoyl peroxide (BPO), ethyl methacrylate (EMA), and methyl methacrylate (MMA). Post soaking, the block was temperature-cured at around 115°C. Hence, this created a CPP structure with the pores being filled by the polymer [21].

- **1c. CPP Infiltrated with a Bonding Polymer:** This time, the CPP block was soaked inside a mixture of benzoyl peroxide (BPO), ethyl methacrylate (EMA), methacrylic acid (MA), and methyl methacrylate (MMA) [21]. The difference between the two polymers is that the non-

bonding polymer (1b) does not have any MA, thus making it hydrophobic (non-polar) and it relies on weaker van der Waals bonds for interaction with the CPP [21]. This polymer (1c), on the other hand, is able to make strong ionic bonds with CPP.

2 . Cutting Speed

Earlier studies had indicated that milling the implant at a maximum cutting speed (i.e., rotating tangential speed) of 22.4 m/min prevented loss of surface porosity [8]. While retaining surface porosity is an important issue in the final use of the implant, the main operation considered in this thesis is roughing. Since roughing is typically followed by semi-finishing and finishing operations, this means that a loss of porosity contained within a layer of limited depth would be acceptable, which could be removed during latter operations. Hence, while earlier studies had considered 10 m/min as an acceptable cutting speed, this thesis will investigate the applicability of a cutting speed range of 10, 20, and 30 m/min for the afore mentioned material scenarios.

3. Chip Load and Depth of Cut

The chip load and depth of cut, in combination, determine the uncut chip area, and therefore the magnitude of forces generated during the machining operation. In thin wall machining, if the force normal to the feed direction becomes excessive, it can result in damage to the wall. Similarly, when the tool is about the exit the implant, the resultant cutting force in the feed direction can cause the remaining bit of material to be broken off before it can be sheared away by the cutting edge. Hence, proper choice of chip load and depth of cut plays a crucial role in avoiding the force overloading and chipping of the implant. Too small values, on the other hand, result in a loss of productivity and increase the cost of the machining operation.

It was stated in [8] that cutting at 0.0125 mm/tooth chip load and 2 mm depth of cut prevented chipping or breakage along the cutting edge of the implant. It is expected that impregnating the CPP with a polymer will change the ductility of the material, so that it can withstand higher cutting forces before breakage occurs. Hence, the following chip loads and depths of cut will be explored in the proceeding studies:

Chip Load: 0.05, 0.10, 0.15 mm/tooth

Depth of Cut: 1, 2, 3 mm

4. Tool Engagement Condition

Tool engagement conditions (i.e., entry and exit angles, as shown in Fig. 3-2) can determine whether the milling operation is up- or down-milling. They also determine the radial width of cut, and the lower and upper boundaries for the uncut chip area [1]. While traditional metal cutting calls for down-milling in finishing operations, to obtain high quality surfaces, in machining CPP it was seen that this mode of operation resulted in the smearing of CPP particles into the pores and therefore the deterioration of surface porosity. Down-milling also has the tendency to generate large impact forces each time a cutting edge engages into the workpiece, which can increase the tendency for breakage or chipping. Therefore, an up-milling configuration consisting of an entry angle of ϕ_{st}=0° was experimentally validated to be more appropriate for milling CPP [8], which resulted in a cutting effect similar to "plucking" out the CPP particles; thereby leaving an open-porous surface post-machining.

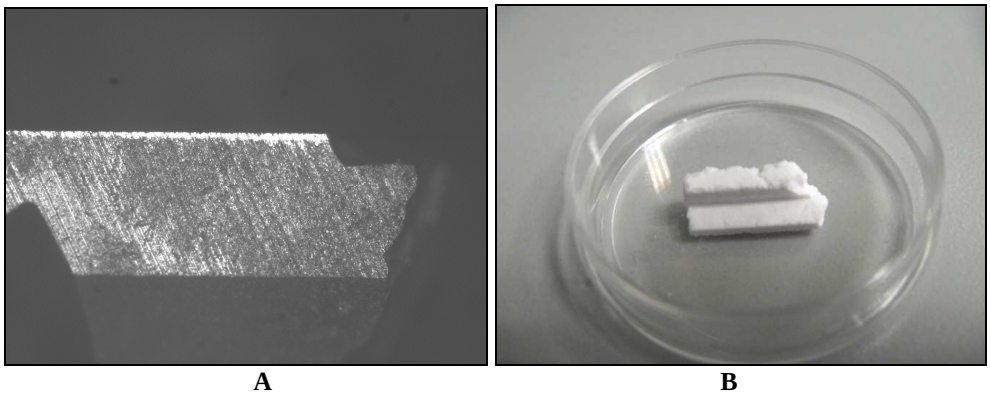

A **B**

Figure 3-3: A: 4 mm Diameter, 4 Flute Flat Endmill (worn-out after 9 experiments), B: Workpiece (Run #2).

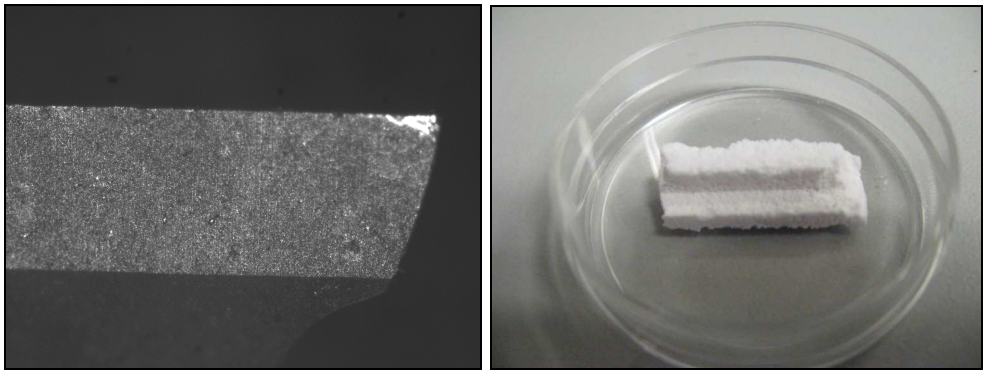

A **B**

Figure 3-4: A: 4mm Diameter, 2 Flute Flat Endmill (very little wear after 9 experiments), B: Workpiece (Run #3).

Although the maximum material removal rate would be obtained when the tool is engaged with its full diameter (i.e. ϕ_{ex}=180°, resulting in "slotting"), when a 4-fluted cutter is considered, as was the original plan when starting out with the "best conditions" reported in [8], it can be verified that this creates the worst-case for triggering chatter vibrations and can cause chipped edges along the implant. To avoid this situation, three quarters immersion was chosen, resulting in an exit angle of an exit ϕ_{ex}=120°. This exit angle was also retained when the cutter type was changed from four fluted to two.

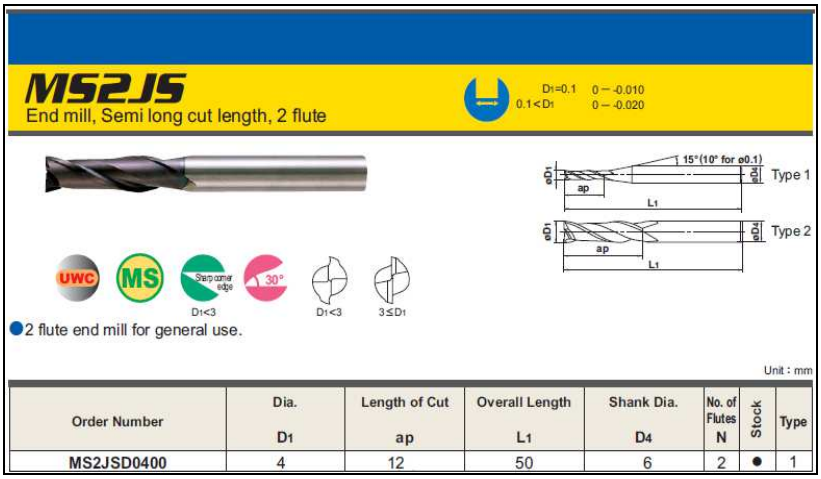

Order Number	Dia. D1	Length of Cut ap	Overall Length L1	Shank Dia. D4	No. of Flutes N	Stock	Type
MS2JSD0400	4	12	50	6	2	●	1

Figure 3-5: Mitsubishi Tool Selected for Cutting Tests

5. Number of Flutes

Although increasing the number of flutes in a milling cutter can help decrease the chip load while keeping the overall feed rate constant, it was found for machining CPP that using a 4 mm

diameter tool with 4 flutes resulted in significant problems with the chip evacuation. As a result, it was observed that the tool wore out prematurely, and the worn tool also caused excessive force loading, which led to breakage in the CPP samples while leaving the cut, as seen in Figure 3-3. By switching to a 2-fluted tool, this problem was avoided and much better surfaces could be produced without wearing out the tool or breaking the part. This is shown in Figure 3-4. Hence, a 2-fluted tool was selected for the remaining machinability studies, which is shown in Figure 3-5.

After setting the engagement conditions and the tool selection as aforementioned, the remaining factors are to be investigated, each of which is considered in three levels, are listed in Table 3-1. The design-of-experiment in Section 3.5 is achieved by considering these factors.

Table 3-1: Factors and Levels for Each Factor.

Factors	Levels		
	1	**2**	**3**
Material	Porous CPP	CPP + non-bonding polymer	CPP + bonding Polymer
Depth of Cut (mm)	1	2	3
Cutting Speed (m/min)	10	20	30
Chip Load (mm/tooth)	0.05	0.1	0.15

Exp. No.	Factors		
	A	**B**	**C**
1	1	1	1
2	1	2	2
3	2	1	2
4	2	2	1

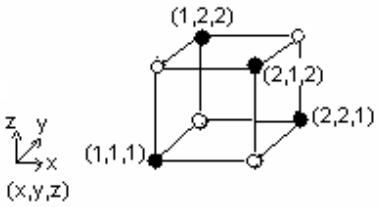

Table 3-2: L_4 (2^3) Orthogonal Array. **Figure 3-6: 3-Dimensional Cube for L_4.**

3.4 Design-of-Experiment Using an Orthogonal Array

This section briefly describes the general process of constructing an orthogonal array for designing experiments. Before generating the array, the following requirements must be defined:

- Number of factors
- Number of levels for each factor
- Interactions between factors to be estimated

- Particular difficulties that would be encountered in running the experiments

Once these have been defined, the minimum number of experiments corresponding to the degrees of freedom must be performed to study the chosen factors and levels for each control factor.

To further explain the construction of an orthogonal array, consider an example of a 2^3-L_4 experiment. Such an experiment would be defined to represent a situation involving 3 factors with 2 levels each. One degree of freedom is associated with the overall mean, regardless of the number of control factors that need to be studied. Table 3-3 indicates the total degrees of freedom for a 2^3-L_4 experiment to be four. A 2-level factor counts as one degree of freedom, because for a 2-level factor (for example, factor A), we are interested in the comparison of two possible cases. By taking A1 as the base level, we want to know how the response changes when we change the level to A2.

Table 3-3: Total Degrees of Freedom Considered in an L_4 Experiment

Factor	Degrees of Freedom
Overall Mean	1
A, B, C	3 x (2-1) = 3
Total	4

The three dimensional cube in Figure 3-2 illustrates coordinates that verify two levels for each factor labeled at the vertices that are of interest for an L_4 orthogonal array. The vertices of interest interact diagonally with each other on every face of the cube. Hence, for every face 2 vertices are eliminated from the experiment, thus parting a total of 4 vertices (4 runs), as shown in Table 3-2. Hence, an L_4 orthogonal array would be a viable choice for this experiment.

Table 3-4: Standard Orthogonal Arrays [3].

Orthogonal Array	Number Of rows	Maximum Number of Factors	Maximum Number Of Levels For Each Factor			
			2	3	4	5
L_4	4	3	3	-	-	-
L_8	8	7	7	-	-	-
L_9	9	4	-	4	-	-
L_{12}	12	11	11	-	-	-
L_{16}	16	15	15	-	-	-
L'_{16}	16	5	-	-	5	-
L_{18}	18	8	1	7	-	-
L_{25}	25	6	-	-	-	6
L_{27}	27	13	-	13	-	-
L_{32}	32	31	31	-	-	-
L'_{32}	32	10	1	-	9	-
L_{36}	36	23	11	12	-	-
L'_{36}	36	16	3	13	-	-
L_{50}	50	12	1	-	-	11
L_{54}	54	26	1	25	-	-
L_{64}	64	63	63	-	-	-
L'_{64}	64	21	-	-	21	-
L_{81}	81	40	-	40	-	-

Generalizing upon this idea, Genichi Taguchi [3] tabulated 18 basic orthogonal arrays, where Table 3-4 lists these 18 standard orthogonal arrays along with the number of columns at different levels. To determine the orthogonal array for the experiments that need to be conducted in this study, the control factors which were determined previously need to be considered. Hence, counting the degrees of freedom of the experiment essentially determines the orthogonal array. In all cases, the overall mean is considered as one degree of freedom.

In the case of identifying the optimum CPP machining conditions, there are only 3-level factors, which are being considered to exhibit a characteristic of only 2 degrees of freedom each (3-1=2). This gives 8 degrees of freedom, and one for the mean, thus summing up to a total of 9 degrees of freedom (i.e., 9 runs), as shown in Table 3-5. Hence, for the identified 4 factors of material, depth of cut, cutting speed, and chip load, the L_9 orthogonal array has been adopted in the design of experiments.

Table 3-5: Total Degrees of Freedom Considered in an L_9 Experiment.

Factor	Degrees of Freedom
Overall Mean	1
A, B, C, D	4 x (3-1) = 8
Total	9

3.5 Design and Execution of Machining Experiments According to an L_9 Array

Design of the experiments is developed to mill the CPP at the highest possible productivity, while ensuring acceptable quality for the manufactured implants.

The process of developing a model with certain control factors that are minimally affected by noise provides reliability in the experiment. Noise factors are classified as external, unit-to-unit variation, and deterioration. Some of the external noise factors are considered to be vibrations of the surrounding CNC machine, as well as the CNC machine and tool itself. A unit-to-unit variation, in this case, is the production of the CPP blocks. They are conventionally sintered to certain dimensions, which can vary from block to block. Material properties, and therefore the machining response may vary from batch to batch. However, due to the limitation of the CPP fabrication resources, CPP block of different compositions were pronounced in the same batches. A deterioration noise factor, in this case, is tool wear. Hence, monitoring the tool wear after each run can help to remove this noise factor from the model.

Table 3-6: L_9 (3^4) Orthogonal Array with Labeled Parameters.

Experiment No.	Factor A Material	Factor B Depth of Cut (mm)	Factor C Cutting Speed (m/min)	Factor D Chip Load (mm/tooth)
1	Porous CPP	1	10	0.05
2	Porous CPP	2	20	0.1
3	Porous CPP	3	30	0.15
4	CPP+ non-bonding polymer	1	20	0.15
5	CPP+ non-bonding polymer	2	30	0.05
6	CPP+ non-bonding polymer	3	10	0.1
7	CPP+ bonding polymer	1	30	0.1
8	CPP+ bonding polymer	2	10	0.15
9	CPP+ bonding polymer	3	20	0.05

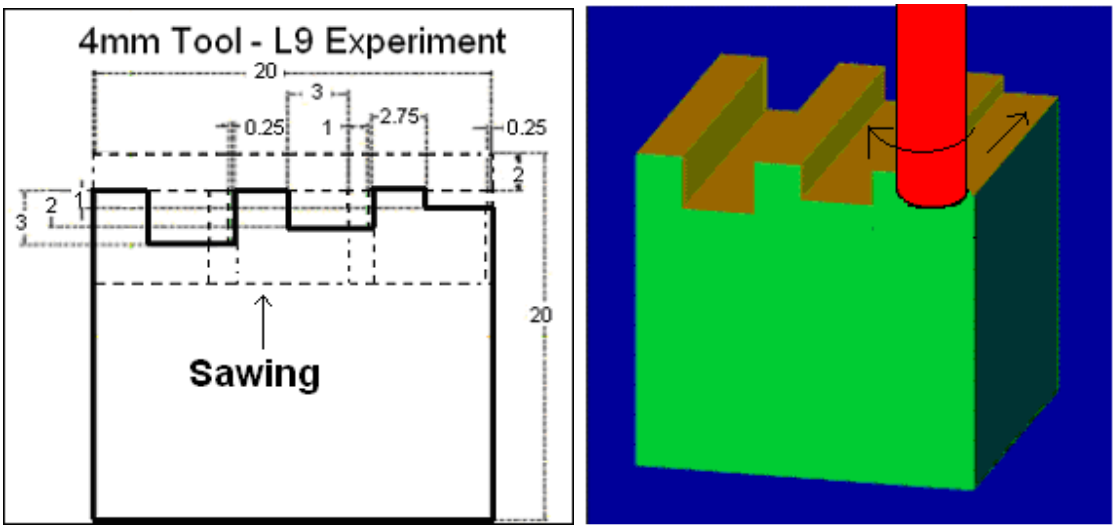

A **B**

Figure 3-7: A: Drawing of a Single Machining Specimen (units: mm), B: Verified Machining Part in MasterCAM.

The experiments in this section were designed to eliminate the conditions that do not fit the objective of high productivity and good quality machining, with particular focus on the roughing process. The response set of interest, for the experiments, is comprised of:

1 – Surface / Feature Integrity

2 – Surface Porosity

The surface and feature integrity will be assessed based on subjective evaluation of visual observations on a scale from 1 to 5, with representing the worst, and 5 representing the best cases. The surface porosity, on the other hand, will be evaluated quantitatively by computing the percentage of surface pore area in obtained Scanning Electron Microscope (SEM) images of machined samples. This will determine the quality of the cuts by distinguishing the better machined specimens from the poor ones. Overall, the experiments will help determine the most significant factors that affect the surface integrity and porosity.

In addition to inspecting the machined specimens for surface integrity and porosity, tool wear of the cutter will also be monitored after each cut for assurance that the tool retains its sharpness. The control factors and settings chosen for each factor of according to the L_9 array are shown in Table 3-6.

The CPP machining test blocks were conventionally sintered according to standard protocol in [18]. The polymer impregnated samples were prepared as explained in Section 3.3. All samples were fabricated by Dr. Eugene Hu at the University of Toronto in the Biomaterials Department. The dimensions of the blocks, post sintering, were 20 mm $\times$ 20 mm $\times$ 20 mm.

Each block will be subject to 3 cuts, where each pass will have different machining parameters obtained from the L_9 orthogonal array. The passes will have equal wall thicknesses (2.75mm) between each other and also 0.25mm for a clearance path. Straightness and integrity of the edges along the wall of the specimens would indicate good surface quality, and as a result, good machinability. Figure 3-7 illustrates the machining layout for each block in the experiment.

After the machining cuts are complete, all three specimens on each block are separated individually with a slitting saw, so they can be imaged thoroughly for surface integrity and surface porosity. A solid carbide slitting saw with 2-3/4” diameter x 1/32” thickness and 72 teeth was used to cut the specimens.

3.6 Analysis and Discussion of Results

A B

Figure 3-8: Comparison Images for Surface Integrity. A: Chipping along edges for Run #4; B: No Chipping Along Edges, Run #9.

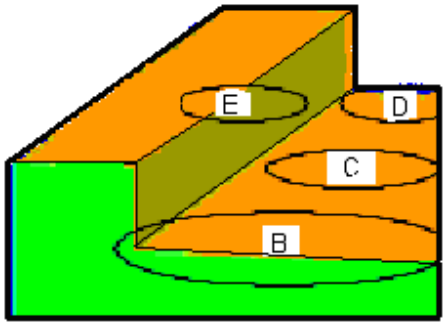

Figure 3-9: SEM Imaging Locations for Each Specimen.

The data summary for all 9 experiments was computed in a similar fashion and the results were tabulated for each response in terms of surface integrity and surface porosity. Once the data was collected, it was analyzed to estimate the effect of each control factor at the level of interest by constructing an analysis of variance (ANOVA) table. Main effects plots were constructed to justify which factor had the most influence on each response. Interaction plots were also constructed to justify which level at every factor had the most influence on surface integrity and surface porosity. These steps are detailed in the proceeding subsections.

3.6.1 Visual and Tabular Evaluation

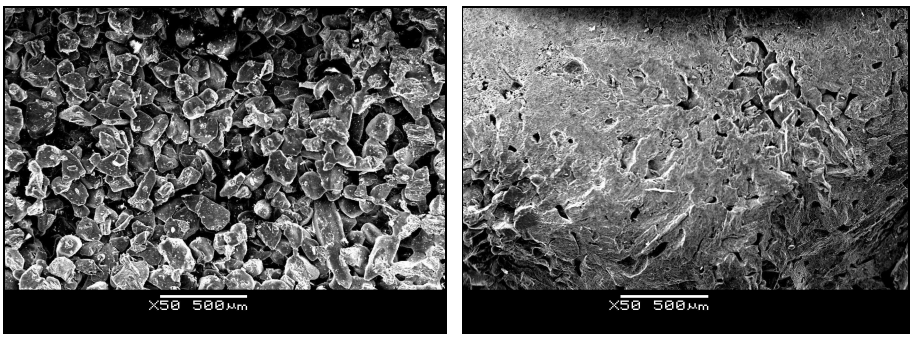

A B

Figure 3-10: Comparison Images for Surface Porosity. A: Good Surface Porosity Obtained in Run #1, B: Significant Loss of Surface Porosity Obtained in Run #4.

The surface integrity was evaluated along different parts of each specimen. Figure 3-8 presents images obtained with a camera. They were taken to verify the quality of surface integrity and used in a subjective evaluation. The images were categorized for the following positions in the cut: when the tool enters the specimen; the inside pocket of the specimen; and when the tool exits the specimen, generating a total of 3 evaluations to obtain an overall summation. Observations for the 3 positions and the overall summations are shown in Table 3-7.

The images illustrate the quality of the specimen and were used to evaluate the surface integrity of the material after each cut. For example, in Figure 3-8A the specimen has more chipping along the edges and would receive a low value of "1" in its category. The specimen in Figure 3-8B has no chipping along the edges it would receive the highest grade of "5".

The SEM images help determine the percentage of surface pores per area in each run. The SEM images were taken at 4 different locations as shown in Figure 3-9; entry of the tool into the specimen (1), middle of the cut (2), tool exit (3), and the inner edge of the specimen (4). These locations have been labeled from B to E, in the mentioned order.

The observations for surface porosity were interpreted by computing the surface pore per area percentage. This was accomplished by processing the SEM images with Image-Pro Plus®, which determined the mean and variance of the pores along the surface of the material by estimating the grayness histogram for the pore sites. For the percentage of surface pores per area,

the higher value indicates better porosity. Figure 3-10 shows a comparison of two different porosity levels that were seen in the experiment. Figure 3-10A has high surface porosity percentage (36.5 %) whereas Figure 3-10B has significant loss of surface porosity, computed as a percentage of 0.9 %. Sample images for Run #1 are shown in Figure 3-11. Images obtained for the other runs are presented in Appendix A.

Table 3-7: Summary of Experimental Conditions and Surface Integrity and Surface Porosity Response Levels.

Exp. No.	**Material**	**DOC** (mm)	**Cutting Speed** (m/min)	**Chip Load** (mm/tooth)	**Surface Integrity at Entry Of Cut**	**Surface Integrity at Exit of Cut**	**Surface Integrity on Inner Edge of Cut**	**Overall Surface Integrity**	**Surface Porosity/ Surface Pore Area** (% Area)
1	Porous CPP	1	10	0.05	4	3	4	**11**	**36.5**
2	Porous CPP	2	20	0.1	3	1	4	**8**	**29.4**
3	Porous CPP	3	30	0.15	3	1	4	**8**	**30.2**
4	CPP + Non-Bonding Polymer	1	20	0.15	2	1	1	**4**	**6.1**
5	CPP + Non-Bonding Polymer	2	30	0.05	1	1	3	**5**	**0.9**
6	CPP + Non-Bonding Polymer	3	10	0.1	4	1	2	**7**	**6.9**
7	CPP + Bonding Polymer	1	30	0.1	4	5	3	**11**	**18.4**
8	CPP + Bonding Polymer	2	10	0.15	4	2	4	**10**	**21.2**
9	CPP + Bonding Polymer	3	20	0.05	5	5	5	**15**	**23.5**

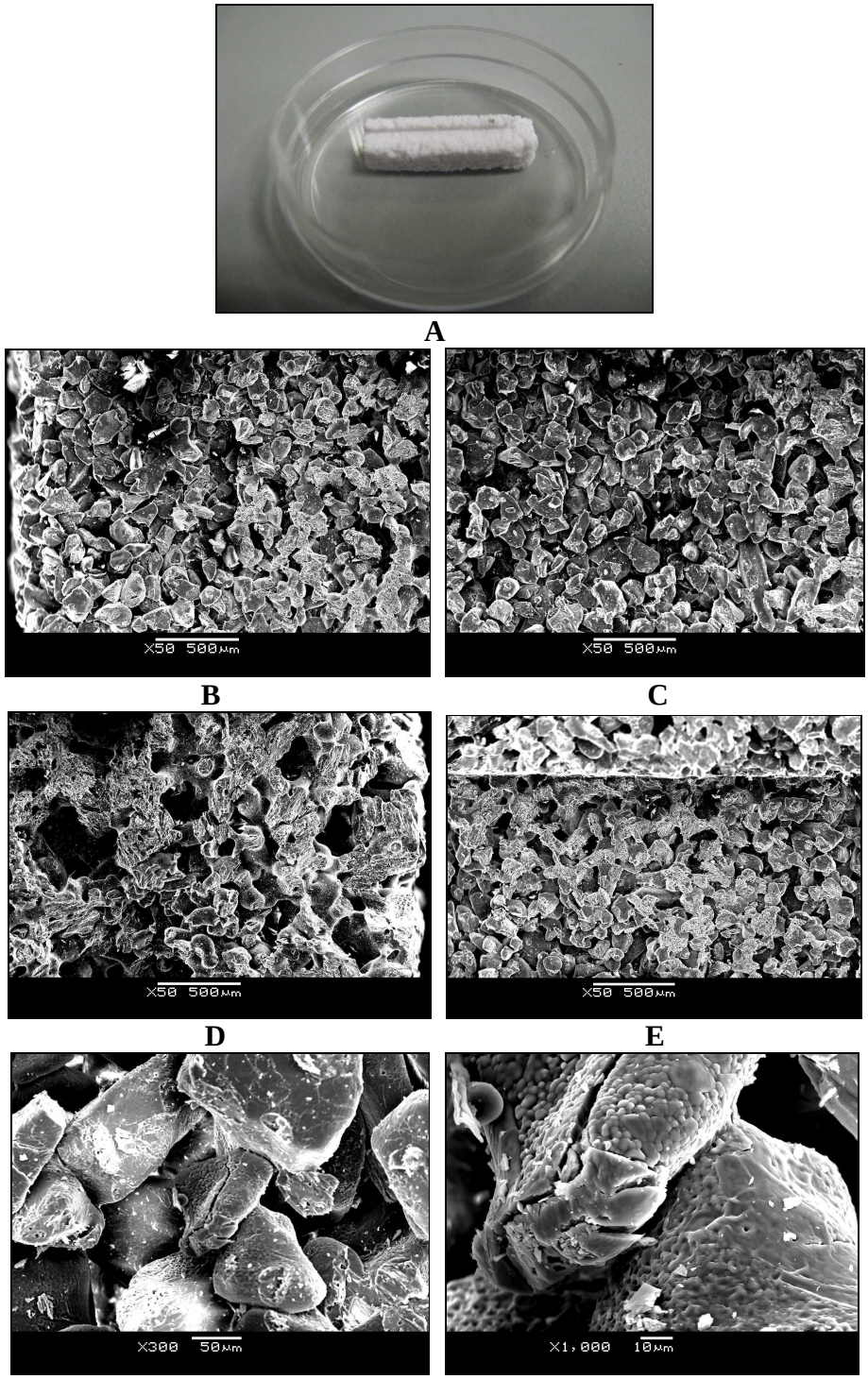

Figure 3-11: Run 1 CPP Non-Infiltrated, Depth of Cut: 1mm, Chip Load: 0.05mm/tooth, Cut Speed: 10m/min (From top left to bottom right. Image A: the Specimen, Image B: Entrance of the cutpass, Image C: Middle of the cutpass, Image D: Exit of the cutpass, Image E: Inner edge of the cutpass, Image F&G: Higher magnification of Image C.

3.6.2 Statistical Analysis and Observations

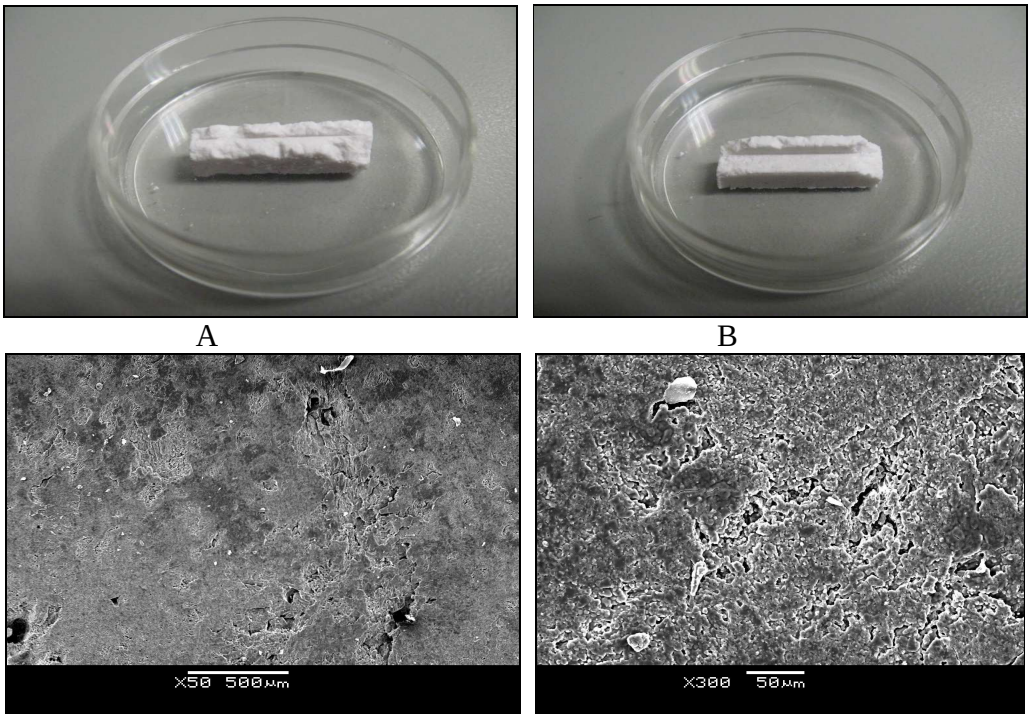

Figure 3-12: A: Run 4 - CPP Infiltrated with the Non-Bonding Polymer, Depth of Cut: 1mm, Chip Load: 0.15mm/tooth, Cutting Speed: 20m/min; B: Run 5 - CPP Infiltrated with a Non-Bonding Polymer, Depth of Cut: 2 mm, Chip Load: 0.05mm/tooth, Cutting Speed: 30m/min; C: SEM image of the middle pass; D: 300X Magnification of Image C.

The responses obtained in all 9 runs are tabulated in Table 3-7. Some of the observations from the experiment are noted in the following:

1. Surface integrity of the non-infiltrated CPP had quite a bit of chipping along the edges of the specimen. This was expected, because the envelope of the experiments started at the upper limits of machinability for unempregnated CPP. Especially where the tool exits the specimen, the edge has high amount of chipping and breakage, as seen in Figure 3-11.

2. Surface porosity is excellent throughout the surface for Run #1 with plain CPP. The higher magnifications (300X and 1000X in Figure 3-11) show that the cavity openings are very large and low smearing occurs on each particle. The obtained surface porosity is acceptable and of practical use for surgical purposes.

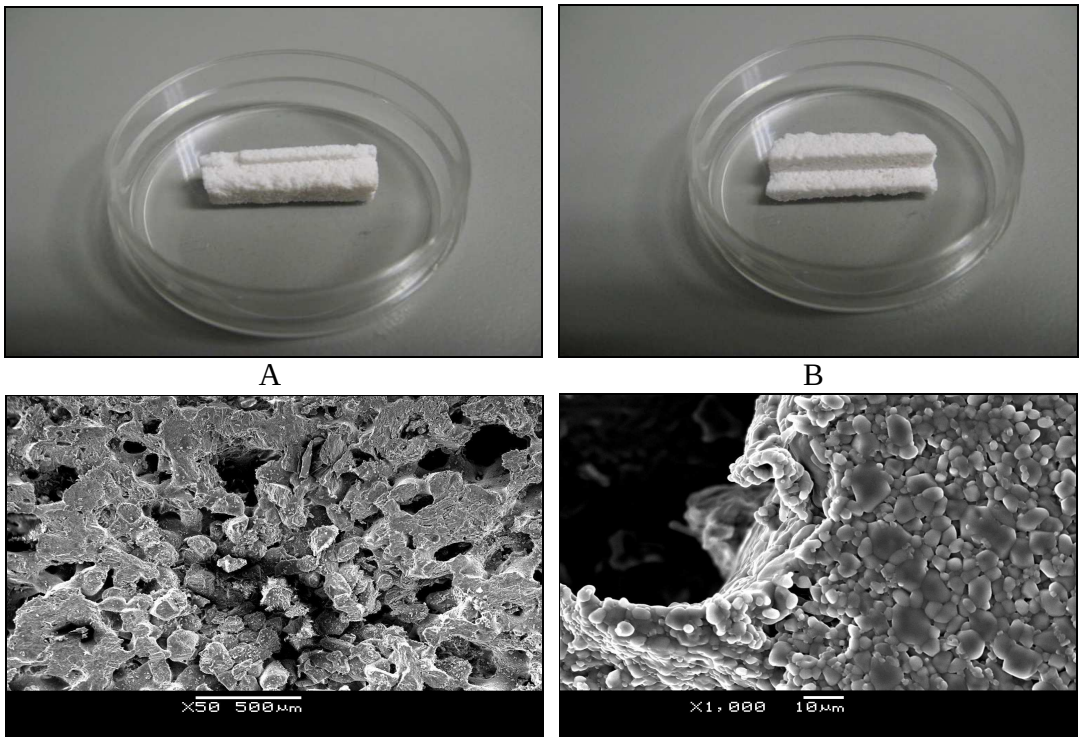

Figure 3-13: A: Run 9 - CPP Infiltrated with a Bonding Polymer, Depth of Cut: 3mm, Chip Load: 0.05mm/tooth, Cutting Speed: 20m/min, B: Run 7 - CPP Infiltrated with a Bonding Polymer, Depth of Cut: 1mm, Chip Load: 0.1mm/tooth, Cutting Speed: 30m/min, C: SEM Image of the Middle Pass, D: 1000X Magnification of Image C.

3. Considering Figure 3-12, the surface integrity and porosity of CPP infiltrated with a non-bonding polymer is very poor. The edges are unacceptable and the material demonstrates extreme loss of surface porosity. It is speculated that the high cutting speed may have contributed to the melting of CPP particles and the polymer, thus generating a smooth and closed surface during cooling. Hence, this material is not suitable for machining CPP implants due to its extreme loss of surface porosity and high chipping, making the implant unusable for its clinical application.

4. The surface integrity of CPP infiltrated with the bonding polymer is much better, when compared to the results obtained with the other 2 materials, as seen in Figure 3-13. The 0.05mm/tooth and 0.1mm/tooth chip loads are the conditions where the least amount of chipping occurs. The 0.05mm/tooth chip load showed excellent results in terms of machinability. The edges were nearly flawless with no sign of chipping. While some areas of the surface had loss of

porosity. However, the research collaborators in the Biomaterials Laboratory at the University of Toronto have indicated that the amount of surface porosity retained was still sufficient to grow cartilage cells on the implant.

The results for surface integrity and surface porosity were gathered to create a statistical analysis, in the form of an Analysis of Variance table (ANOVA) [3]. These tables, shown in Table 3-8 and Table 3-9, determine the outcome variances caused by each factor. The ANOVA was developed by calculating the response for each factor at each separate level. Then, the sum of squares was calculated to determine the mean of squares. The mean square per standard error for every factor would determine whether that factor would be within the confidence interval of the mean. If the case is such that the influence of a factor is past a critical point, then that factor would be considered as the cause for the variation of that response. Upon this, "main effects plots" are developed to validate the influence of the factors in each response. Figure 3-14 illustrates the main effect plots for surface integrity and Figure 3-16 illustrates the main effect plots for surface porosity. Also, "interaction plots" are developed to justify the most optimal level for each factor of significance to the response.

Table 3-8: ANOVA Table for Surface Integrity with 95% Confidence Interval, f-cr.(α=0.05) = 6.94.

Factor	Level 1	Level 2	Level 3	Degrees of Freedom	Sum of Squares	Mean of Squares	F obs.
A-Material	9.00	5.33	12.00	2	66.89	33.44	**12.04**
B-DOC	8.67	7.67	10.00	2	8.22	4.11	1.48
C-Cut Speed	9.33	9.00	8.00	2	2.89	1.44	0.52
D-Chip Load	10.33	8.67	7.33	2	13.56	6.78	2.44
Error				0	0	0	
Total				8	91.56		
(Error)-pooled estimates				4	11.11	2.78	

According to the analysis of variance table, the most significant factor affecting the surface integrity is material. Also, by looking at the main effect plots, it can be seen that the chip

load has a moderate effect on surface integrity. Cutting speed and depth of cut seem to have much smaller, almost negligible, effects on this outcome.

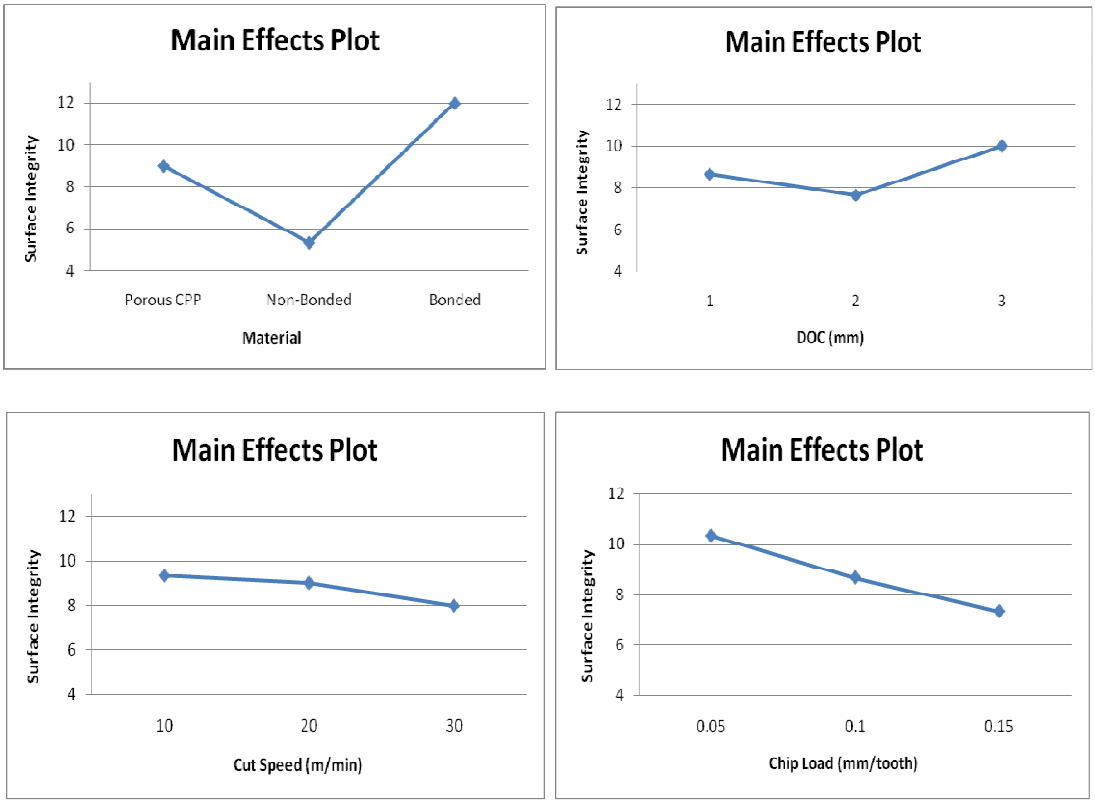

Figure 3-14: Main Effect Plots for Surface Integrity.

The interaction plots verify that setting the conditions of the material factor to CPP with a bonding polymer will provide the optimal cutting performance for surface integrity in the model. Hence, infiltrating the CPP with polymers that achieve ionic bonding with the scaffold provides a simple and efficient method to improve the machinability of the material. Infiltrating with a polymer that realizes only van der Vals bonds with CPP, on the other hand, leads to a poor surface integrity and does not help to achieve more productive cutting conditions.

The interaction plots for material show synergistic behavior, implying that CPP with a bonding polymer seems to be the best choice. The interaction plots for chip load, however, show antisynergistic interaction, meaning that an optimum level for this parameter is not really applicable for surface integrity.

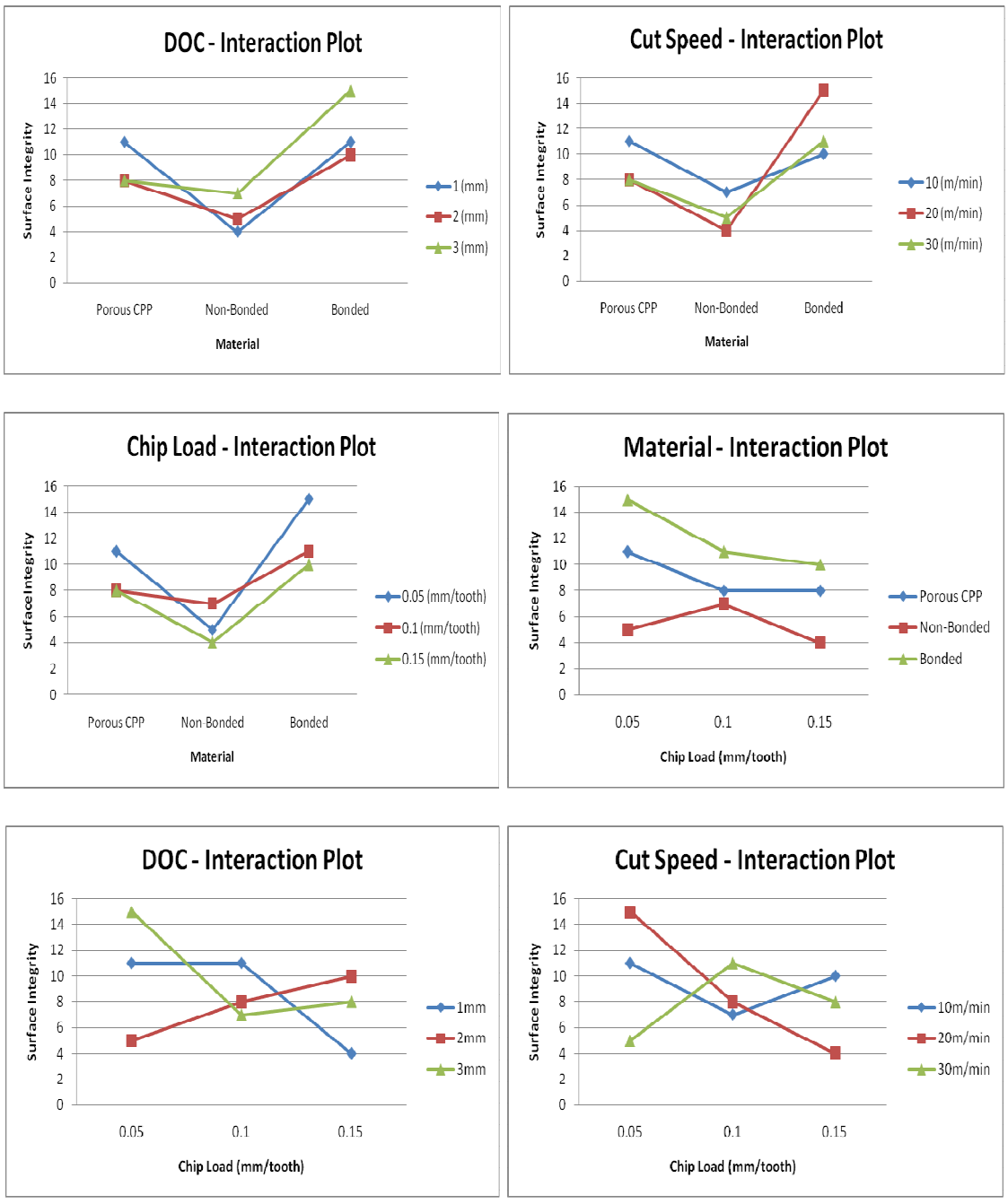

Figure 3-15: Interaction Plots for Surface Integrity.

Table 3-9: ANOVA table for surface porosity with a 95% Confidence Interval f-cr (α=0.05) = 6.94.

Factor	Level 1	Level 2	Level 3	Degrees of Freedom	Sum of Squares	Mean of Squares	Fobs.
A-Material	32.03	4.63	21.03	2	1140.72	570.36	88.86
B-DOC	20.33	17.17	20.20	2	19.25	9.62	1.5
C-Cut Speed	21.53	19.67	16.50	2	38.85	19.42	3.03
D-Chip Load	20.30	18.23	19.17	2	6.43	3.21	0.5
Error				0	0	0	
Total				8	1205.24		
Standard Error				4	25.67	6.42	

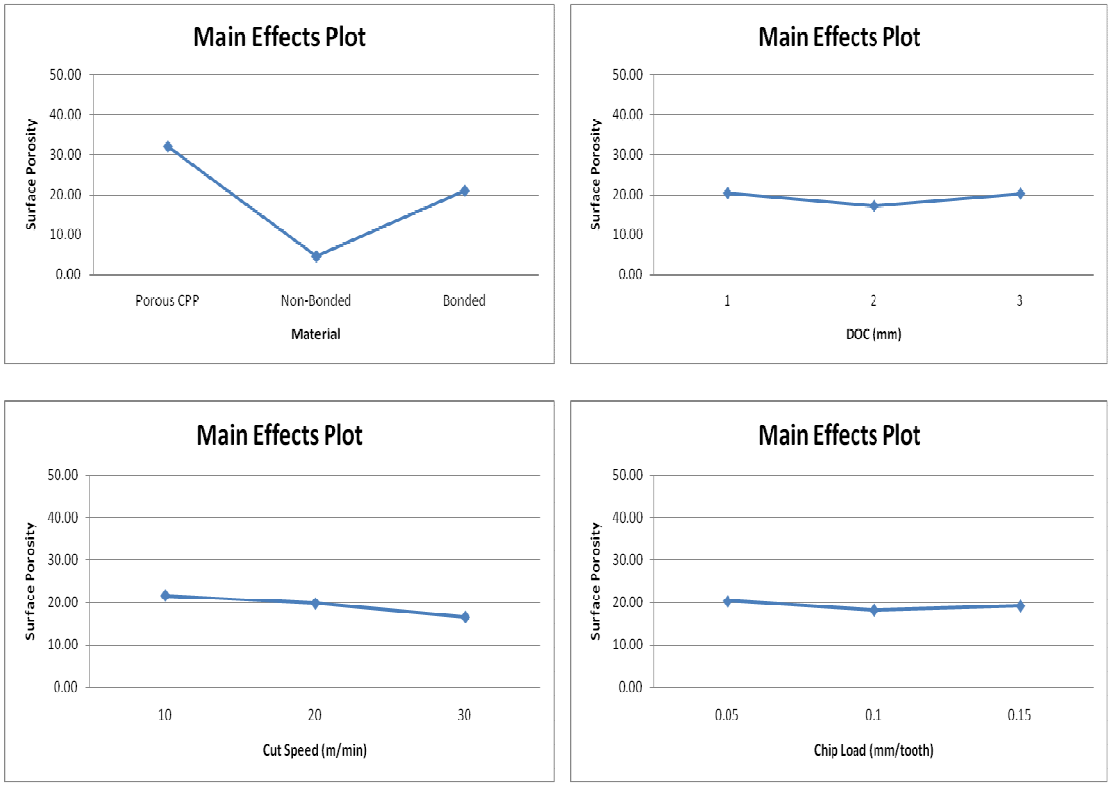

Figure 3-16: Main Effect Plots for Surface Porosity.

According to the analysis of variance in Table 3-9, and the main effects plot in Figure 3-16, the most significant factor affecting surface porosity is material as well.

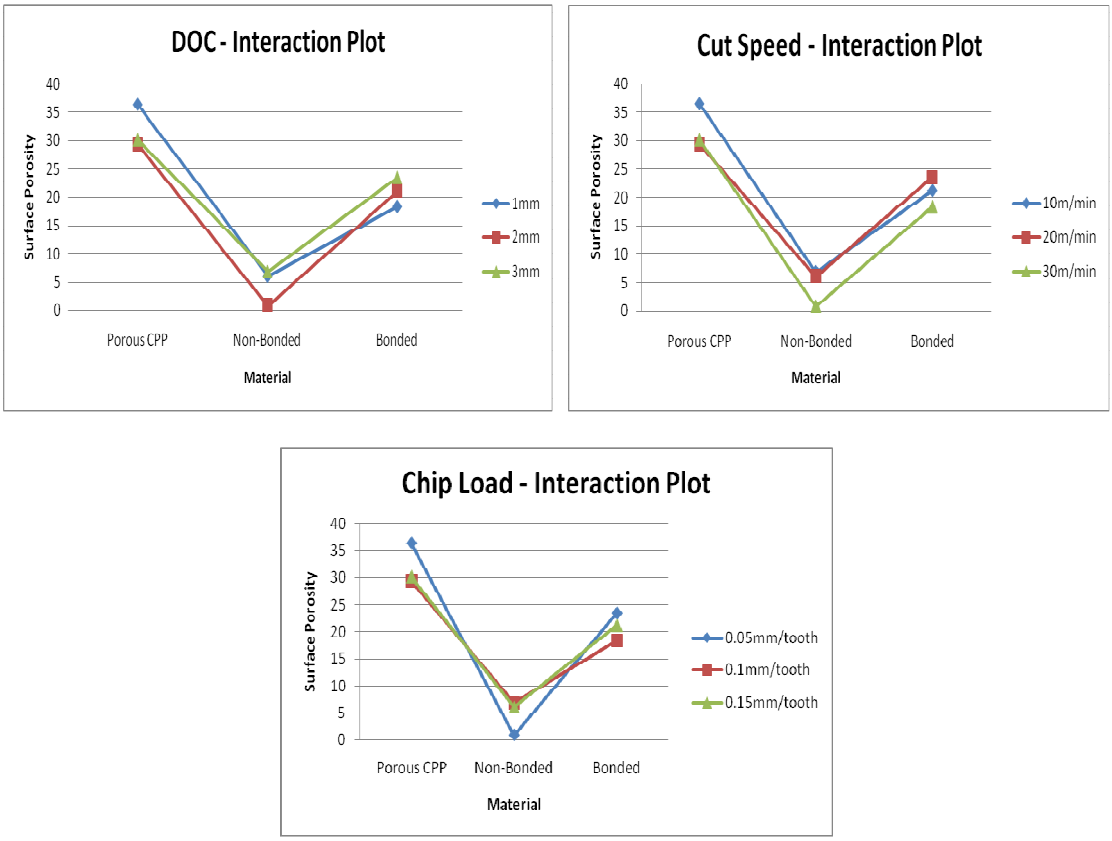

Figure 3-17: Interaction Plots for Surface Porosity.

The non-infiltrated CPP retains the highest surface porosity after machining, compared to the other two materials. This is consistent with the visual and SEM observations noted from each run. Setting the cutting speed to 10m/min seems to develop the highest level of surface porosity. The interaction plots of material and every other factor for surface porosity have synergistic interaction, meaning that the optimum levels identified by the model are applicable and that the material choice has a strong effect on the outcome of surface porosity.

The CPP infiltrated with a bonding polymer also shows sufficient surface porosity. It is possible that the surface porosity is reduced due to the polymer melting and re-solidifying between the CPP particles, thus leaving a few sections of smeared surfaces. Since prior to cell seeding, the polymers are to be burned-off in heat treatment of the implant, the surface porosity can likely be recovered. Furthermore, while surface porosity may be lost to a certain depth

during a rough machinig operation, this layer can later be trimmed off during finish or semi-finish machining.

Overall, the surface integrity response indicates that CPP infiltrated with an ionic bonding polymer seems to be the best choice of material for shaping the implant at high productivity rates.

3.7 Conclusions

This chapter has investigated the design-of-experiment for identifying the most critical factors that influence the surface integrity and porosity in machining CPP. By applying Taguchi's orthogonal array method, followed by visual and SEM imaging and statistical analysis, it was determined that CPP infiltrated with an ionic bonding polymer produces the best material for generating high quality machines surfaces and features. While there is some loss in surface porosity, in comparison to cutting uninfiltrated CPP, the porosity loss was deemed acceptable for the clinical purpose of the implant, and in many cases, would be trimmed off during a consecutive finish machining operation.

Having determined the most suitable material configuration, the next chapter will refine in further detail the remaining cutting parameters for machining CPP.

CHAPTER 4

Further Refinement and Modeling of Machining Conditions and Experimental Validation in Rough Machining of a Tibial Plateau Implant

4.1 Introduction

The earlier chapter had indicated that using CPP which is infiltrated with an ionic bonding polymer as the workpiece material can significantly improve the productivity and surface quality achieved during the roughing operation. This chapter aims to:

- Further refine the machining conditions (Section 4.2.1);
- Construct and verify a mechanistic cutting force model for this material (Section 4.2.2);
- Analyze the stresses and deflection on the implant using Finite Element technique (Section 4.3)
- Validate the optimized cutting conditions and achieved productivity gain by experimentally completing the rough machining cycle for the tibial plateau implant (Section 4.4).

The conclusions for the chapter are presented in Section 4.5.

4.2 Refinement of Cutting Conditions

In Chapter 3, it was determined that impregnating CPP with an ionic bonding polymer can significantly improve the machinability of this material and help obtain excellent surface integrity, as well as acceptable surface porosity. The bonding polymer essentially helps increase the ductility of the composite implant, thereby allowing it to withstand higher cutting forces and impacts during machining. Having chosen the machining material, the objective in this section is to further refine the remaining conditions to maximize the material removal rate.

The parameters that affect the material removal rate during rough milling are:

1) Cutting speed,

2) Engagement condition (i.e., exit angle) of the tool,

3) Chip load, and

4) Depth of cut.

Since surface integrity and high material removal rate are greater concerns than surface porosity in roughing, the cutting speed that will be considered in the proceeding studies is the maximum value (30 m/min) that was used in the earlier experiments in Chapter 3. This speed had still produced implants with acceptable surface porosity. This leaves three other factors to be investigated, which will be realized by considering two levels for each factor, thereby leading to an L_4 design-of-experiment.

4.2.1 L_4 Experiment Design and Execution

Table 3-2 shows an L_4 array which consists of three factors, with two levels designated to each factor [3]. Here, these factors would correspond to exit angle, chip load, and depth of cut. The following levels are considered for each factor:

1. Tool engagement condition (exit angle)

Tool engagement affects the material removal rate, and also the shape of the force profile during and material removal process. While ϕ_{ex}=120° generates a larger uncut chip area and

better material removal rate, a second level of ϕ_{ex}=90° was also chosen to see whether surface quality would be influenced by a reduction in the exit angle.

2. Chip load

Chip load is essential for increasing the material removal rate. Given the surface integrity results obtained in Section 3.5, chip loads of 0.05 and 0.10 mm/tooth seem to generate cuts with excellent surface integrity. Hence, these values have been chosen for the two levels that will be studied further.

3. Depth of cut

Increasing the depth of cut also increases the material removal rate. The results obtained in Section 3.5 show that depth of cuts of 2 mm and 3 mm generate excellent surface integrity. Therefore, these values have been chosen for this study.

The tool (2 flute, 4mm solid carbide end mill) that was used in the experiments in Chapter 3 will continue to be used in the proceeding L_4 experiments. The three factors and two levels that are investigated for each factor are summarized Table 4-1.

To obtain a robust model, these L_4 experiments will be repeated 3 times for each case.

Table 4-1: Orthogonal Array with Control Factors and Milling Conditions.

Experiment No.	**Depth of Cut** (mm)	**Exit Angle** (°)	**Chip Load** (mm/tooth)
1	2	90	0.05
2	2	120	0.1
3	3	90	0.1
4	3	120	0.05

4.2.2 Cutting Force Model

A cutting force model was developed to determine the loads for each run during the next set of experiments. This model determines whether the measurements obtained can also be predicted with cutting mechanics-based simulations.

The force measurements were obtained using MALDAQ software, which is part of the CutPro 7.0 machining process simulation and analysis package. A National Instruments data acquisition card was used to record the force measurements obtained using a Kistler table top dynamometer. In collecting raw data, a sampling frequency of 10 kHz was used without any filtering. The measurements were later processed in Matlab with a 2nd order Butterworth low-pass filter at a cut-off frequency of 250 Hz. CutPro 7.0 was also used to simulate the expected cutting forces using the technique described in [1].

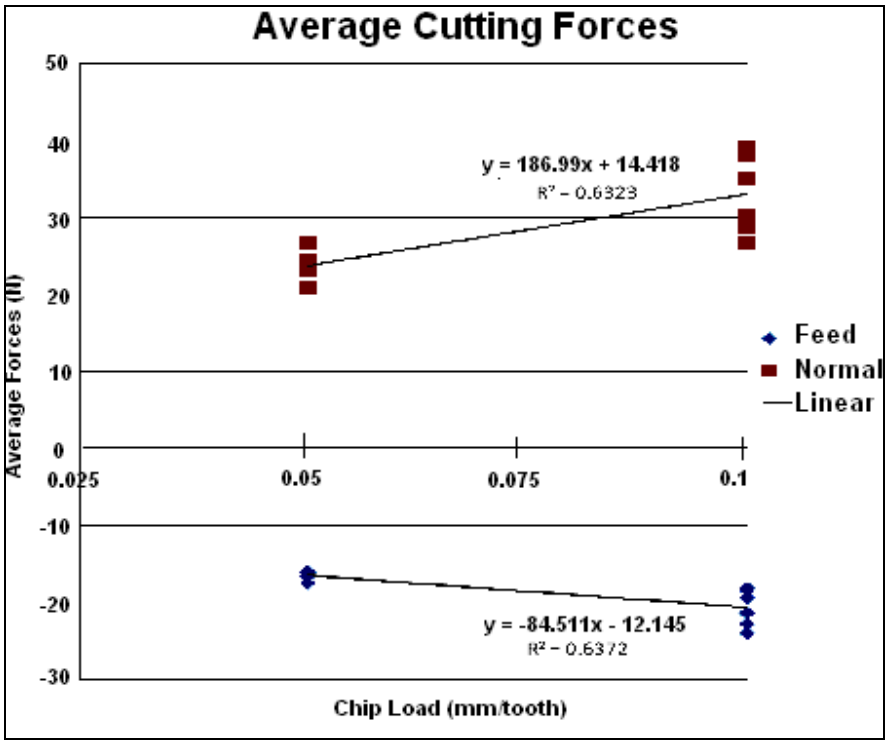

Figure 4-1: Average Forces and Linear Regression for Results on Cutting Tests L_4.

Table 4-2: Identified Cutting Force Coefficients for Impregnating CPP With a Bonding Polymer.

Ktc (N/mm^2)	Krc (N/mm^2)	Kte (N/mm)	Kre (N/mm)	Correlation Coefficients
186.99	84.51	11.32	9.53	$R^2y = 0.632$ $R^2x = 0.637$

The measured average cutting forces and identified cutting force coefficients are shown in Figure 4-1 and Table 4-2. In identifying the cutting force coefficients, the linear fits were applied by considering all 12 experiments (4 tests repeated three times each). The spread of data and

relatively low correlation coefficients are attributed to the non -homogeneous nature of the material [16].

The cutting forces were simulated in both x (feed) and y (normal) directions. The simulations overlaid on top of the experimental data show a close match, indicating reasonably successful identification of the cutting force coefficients and milling behavior of CPP under the tested conditions. It is inevitable that vibrations from the machine tool, surroundings, and the process will also influence the cutting operation, which is the main reason the low-pass filter was used in evaluating the data.

Figures 4-2 to 4-5 show the results for the first run of the Experiments 1 to 4 in Table 4-1. The results for the consecutive repetitions are presented in Appendix B.

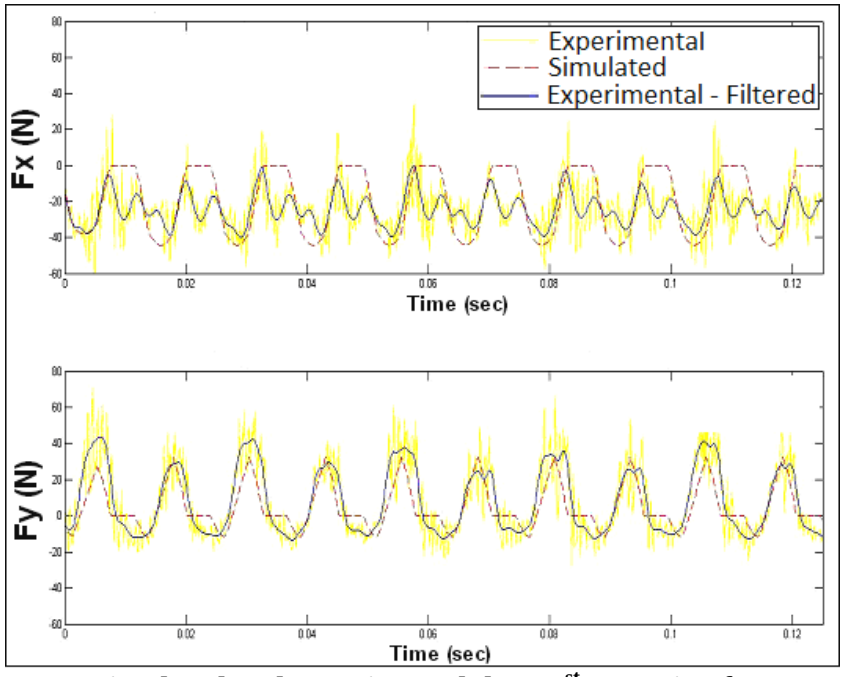

Figure 4-2: Run 1 simulated and experimental data, 1st execution for 4mm, 2-flute flat endmill at 30m/min cut speed, 0.05mm/tooth chip load, and 2mm DOC, half immersion.

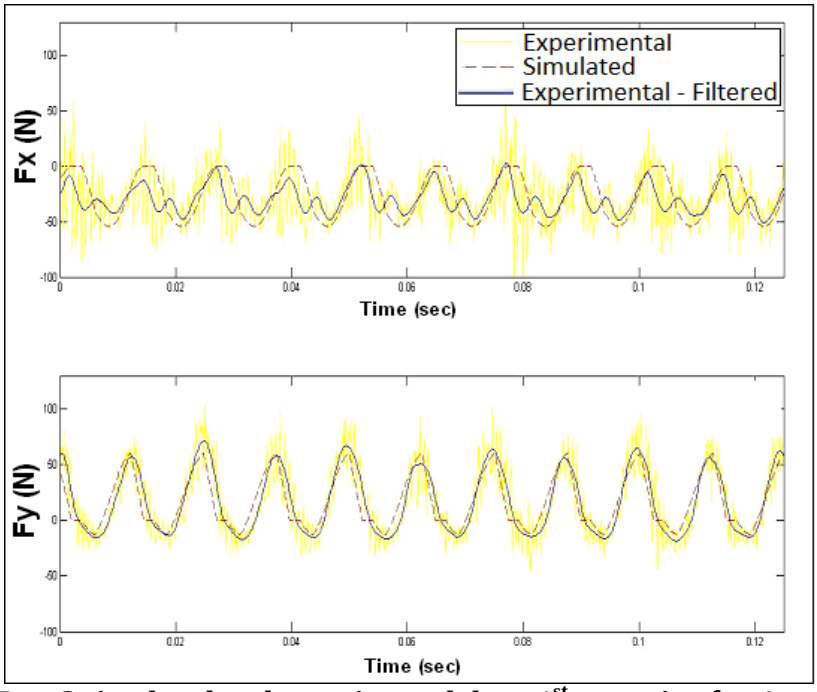

Figure 4-3: Run 2 simulated and experimental data, 1st execution for 4mm, 2-flute flat endmill at 30m/min cut speed, 0.1mm/tooth chip load, and 2mm DOC, 3 Quarter immersion.

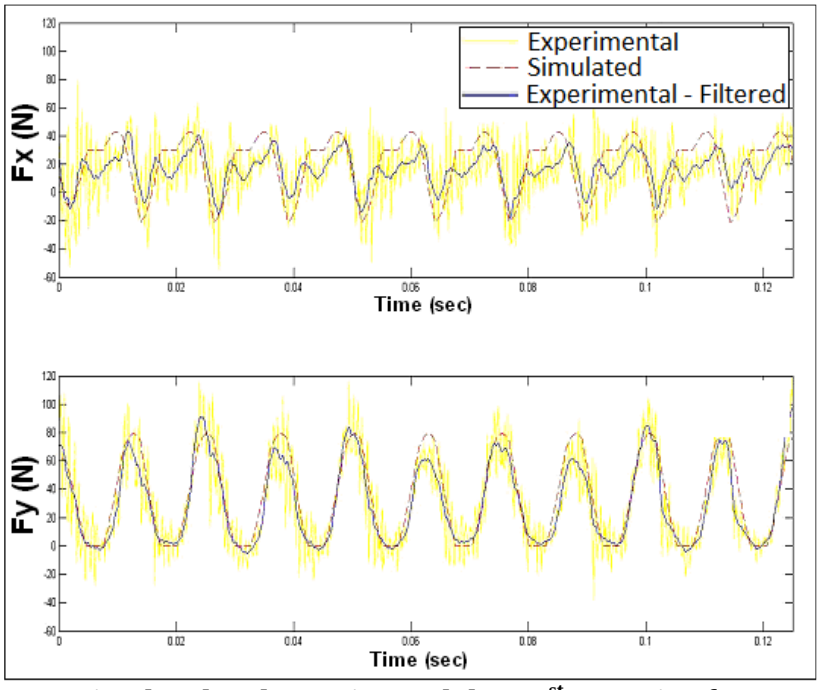

Figure 4-4: Run3 simulated and experimental data, 1st execution for 4mm, 2-flute flat endmill at 30m/min cut speed, 0.1mm/tooth chip load, and 3mm DOC, half immersion.

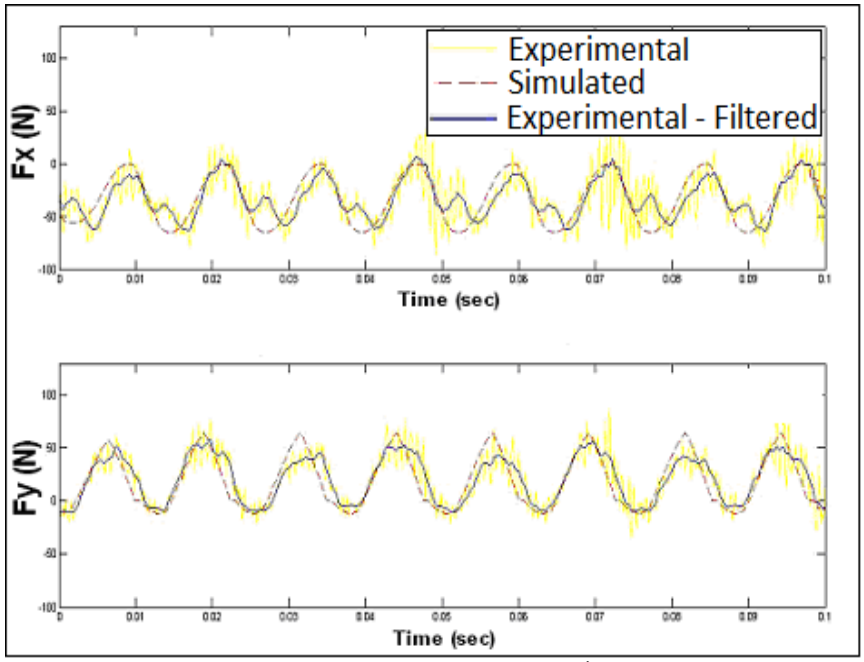

Figure 4-5: Run 4 simulated and experimental data, 1st execution for 4mm, 2-flute flat endmill at 30m/min cut speed, 0.05mm/tooth chip load, and 3mm DOC, 3 Quarter immersion.

4.2.3 Visual and Tabular Evaluation of Results

Surface integrity was evaluated along different parts of each specimen. Images were taken to verify the quality of surface integrity and used in subjective evaluation following the same scaling used in Section 3.6. The cuts in every experiment, conducted three times each, showed no sign of chipping at the edges of the specimen. Hence, all experimental outcomes were evaluated with the highest score of 5, as shown in Table 4-3. The images obtained for each run in the second and third run are presented in Appendix C. Sample images for the first execution are shown in Figure 4-6.

Table 4-3: Observation Chart for First Execution of the L_4 Experiment.

Exp. No.	DOC (mm)	Exit Angle (°)	Chip Load (mm/tooth)	Observation - Surface Integrity		
				1st Repetition	2nd Repetition	3rd Repetition
1	2	90	0.05	**5**	**5**	**5**
2	2	120	0.1	**5**	**5**	**5**
3	3	90	0.1	**5**	**5**	**5**
4	3	120	0.05	**5**	**5**	**5**

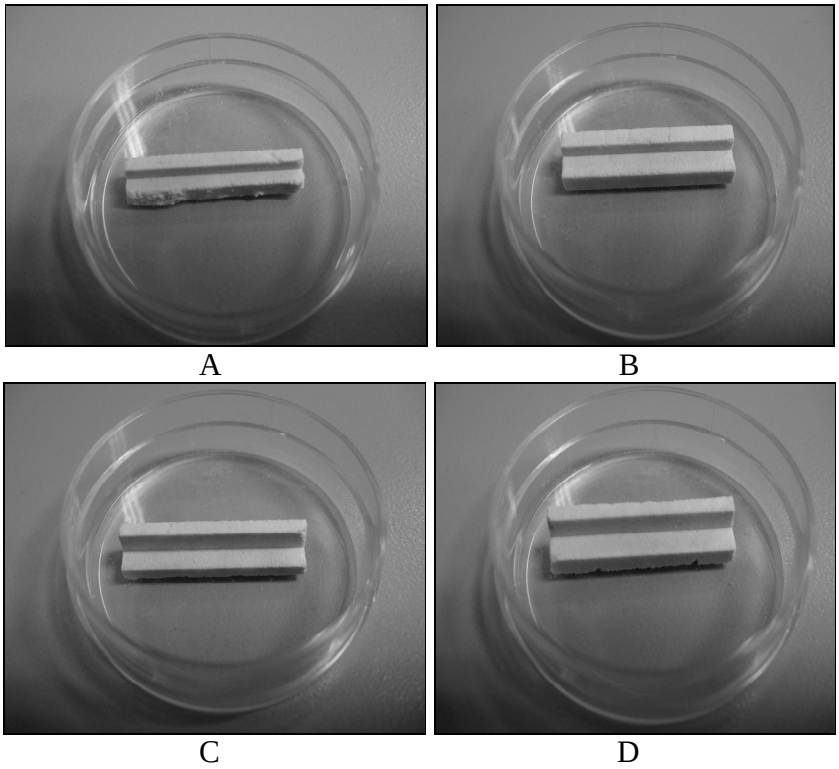

Figure 4-6: Surface Integrity Result for the First Execution of the L_4 Experiment.

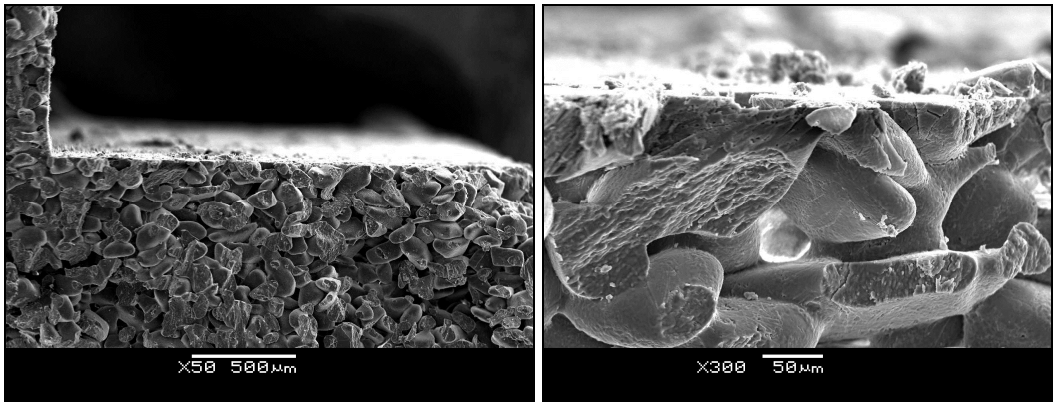

Figure 4-7: Scanning Electron Microscope Images at 2 Different Magnifications of a Specimen from the L_4 Experiment.

In evaluating the results of the L_4 experiment, a statistical analysis was not deemed necessary for identifying the optimal machining conditions, as the choice of highest chip load, largest depth of cut, and largest exit angle still produced excellent surface integrity while maximizing the material removal rate.

While surface porosity is not an issue during the roughing process, it is still a concern how deep into the surface the CPP particles smear during cutting at high speeds nearing 30 m/min. In Appendix A, SEM images taken from runs 7 to 9 illustrate that smearing does indeed occur and is something to watch out for when planning the roughing operation. It should be possible to remove such a smeared layer in a consecutive finishing or semi-finishing operation without having to take additional passes.

To validate that the smearing produced during the L_4 experiments were kept within acceptable limits, a cross-section of a specimen from Experiment #2 was used for SEM imaging. The result is shown in Figure 4-7, which illustrates that the smeared particles go into the specimen only as deep as 50 μm. During the semi-finishing and finishing of the implant, the maximum depth of cut is approximately 1.3 mm, thus removing more than enough material to obtain sufficient surface porosity. The cutting speeds in the semi-finishing and finishing processes are adjusted to be lower, in order to obtain good surface porosity.

4.3 Validation of Cutting Conditions in Finite Element Analysis

It is important to validate that the internal stresses caused by machining forces acting on the implant do not cause the implant to break or chip at a location other than tool contact interface. Therefore, a Finite Element model of the implant was developed in Autodesk, Multiphysics Simulation 2012, and stress analysis was carried out as explained in the proceeding section.

1. Material Properties and FE Mesh

The implant to be machined is composed of 70% density CPP with 75-150 μm particle size, which has been infiltrated with an ionic bonding polymer. Since the polymer impregnation for CPP is a relatively new topic of study, at the time of writing of this thesis, there was no exact data available on the properties of this composite being investigated in the machining studies. While there has been published work on a similar polymer infiltration for CPP [21], it was noted by our collaborator (Prof. R.M. Pilliar) that the properties of the current material under

investigation are likely to be different from those reported in [21]. Therefore, as a conservative assumption, the known material properties for pure and un-infiltrated CPP with 70% density CPP with 75-150 μm particle size were considered in the FE studies, which are shown in Table 4-4.

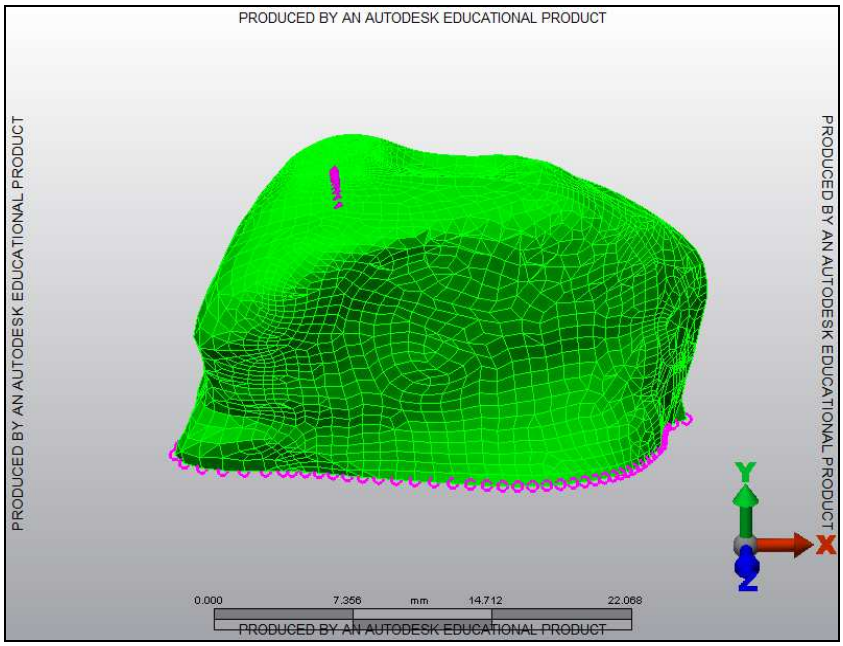

Figure 4-8: Finite Element Mesh used for Stress Analysis.

Table 4-4: Material property data for Finite Element Analysis

Material	Young's Modulus	Mass Density	Poisons ratio
Porous CPP	72 GPa	0.0026 kg/mm³	0.3

The FE model was setup with 4,857 solid mesh elements, where the size of each element was approximately 1.10 mm. The FE mesh is shown in Figure 4-8.

2. Boundary and Loading Conditions

During the actual machining operation, the implant is glued to an aluminum beam for fixturing. To simulate this, the nodes at the bottom portion of the implant were constrained from any motion in the translational x-y-z directions.

Considering the cutting force profiles shown in Figure 4-9, which correspond to 0.1 mm/tooth chip load, 3 mm depth of cut, ¾ immersion, and 30 m/min cutting speed, it can be seen

that the maximum magnitudes of cutting force in the feed and normal directions are approximately 90 N and 40 N, respectively. Hence, a maximum resultant cutting force of around 98.5 N (~100 N) is expected with a 42° angle into the machined wall surface. In a 2-fluted cutter, only one cutting edge will be in contact with the work material at a time. Hence, the resultant force was applied by distributing it along the contacting edge of the helical cutter, shown in Figure 3-3. The force loading onto the implant is shown in Figure 4-10.

The cutting load was applied at different points on the top surface of the implant, where the part is the weakest and chips the easiest. The results were evaluated for each case. As the tool cuts in the vicinity of a smaller protrusion (like the topmost layer for the roughing part), the stress concentration at this protrusion will increase. This can cause the implant to chip and develop form errors, which can also lead to the loss of dimensional accuracy which may not be correctible in consecutive finishing passes.

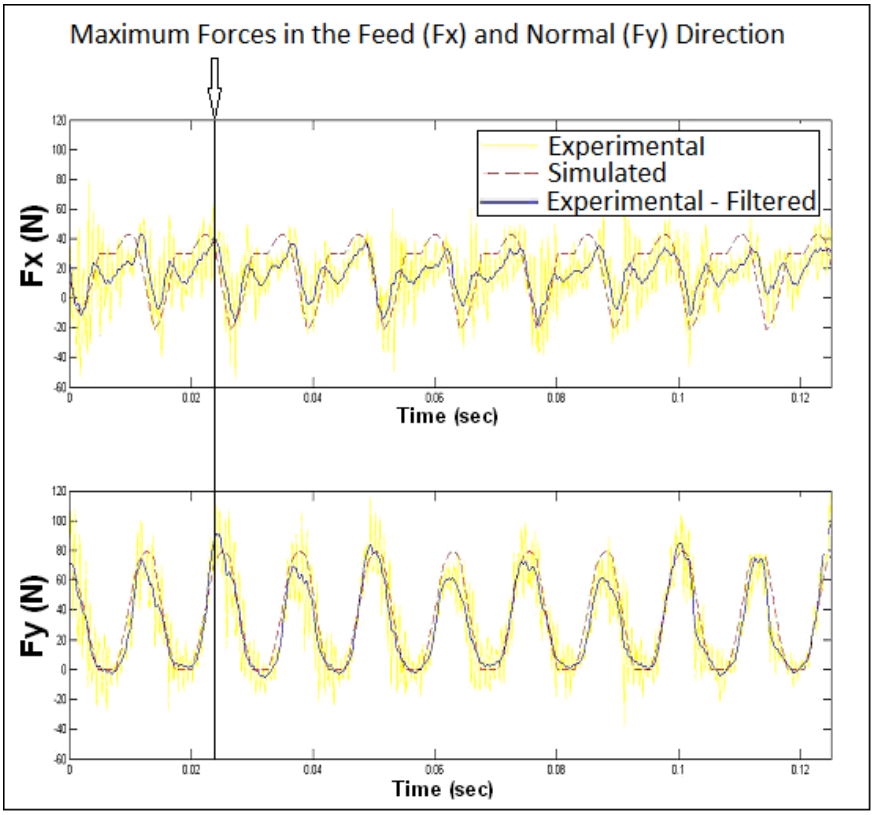

Figure 4-9. Determination of Maximum Forces in the Feed and Normal Directions.

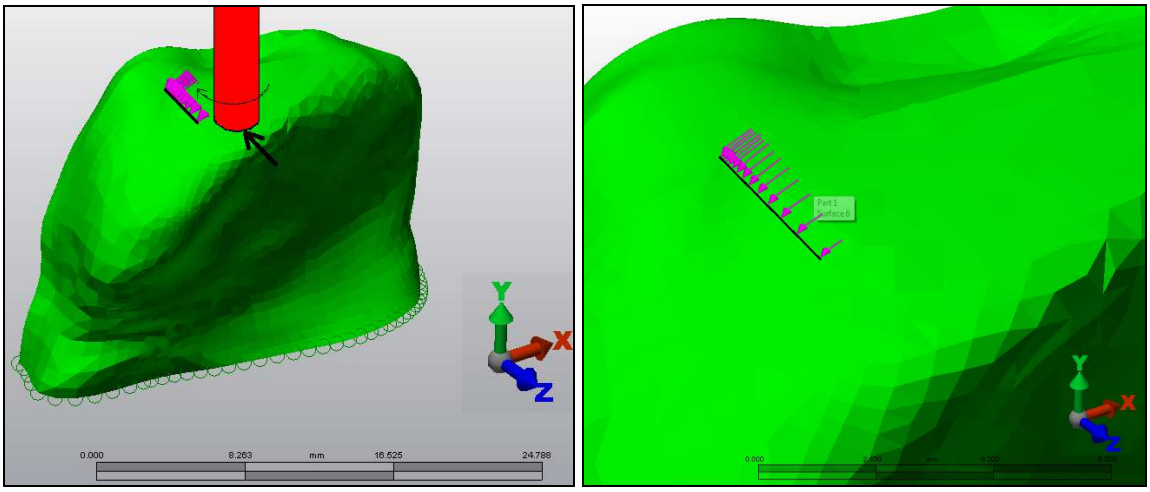

Figure 4-10. Loading Conditions as a Distributed Line Force Acting on the Implant along the Contacting Edge of the Helical Endmill [1].

3. Analysis Method and Results

In carrying out the analyses, Von Mises criterion was used for maximum stress. This is because CPP is known to fracture in a brittle manner rather than show any plastic deformation. To gauge whether the part geometry would be adversely affected by elastic deformations of the implant, the maximum displacement was also evaluated. A sample result from the analyses is shown in Figure 4-11. As can be seen, the highest stress level occurs at the tool contact edge, which is predicted to be around 347 MPa. By applying basic orthogonal cutting mechanics to the cutting coefficients identified in Section 4.2 [1], the friction angle (β_a), shearing angle (ϕ_c) and shear strength (τ_s) were roughly estimated to be β_a=29.3°, ϕ_c=32.9°, τ_s=60.3 MPa [1]. As the predicted peak stress is clearly above the shearing limit, this indicates that main fracture mechanism is the chip removal process due to machining.

There is a notable stress gradient in the outer vicinity of the tool contact edge, which is estimated to be 34-70 MPa. While the machining experiments with uninfiltrated CPP had displayed chipping under the corresponding machining conditions, it was experimentally observed that the ionic bonding polymer infiltrated CPP was able to withstand these stresses

without surface breakage. This is attributed to the pure 70% dense CPP possessing a compressive strength of 38 MPa [8], which is lower than the predicted stress loading. On the other hand, the maximum strength measured through 3-point bending tests for CPP infiltrated with an ionic bonding polymer similar to the one used in this thesis was reported as 87.4 ± 5.1 MPa [21]. Hence, it is believed that the infiltrated CPP samples tested in the cutting experiments also possessed a comparable, or possibly higher, maximum strength.

Elsewhere in the implant, no other stress concentrations are seen which indicate that the implant would not break due to moment overload (i.e. bending) or shearing during the roughing operation.

In addition, the maximum deflection, shown in Figure 4-12, is predicted to be around only 2 microns. This indicates that the elastic deflection is not a major issue that can cause tolerance violations during rough machining, since another 1.3 mm of material would typically be removed by a proceeding semi- and final-finishing operation. Key results of the FE studies, obtained for the worst-case point have been summarized in Table 4-5.

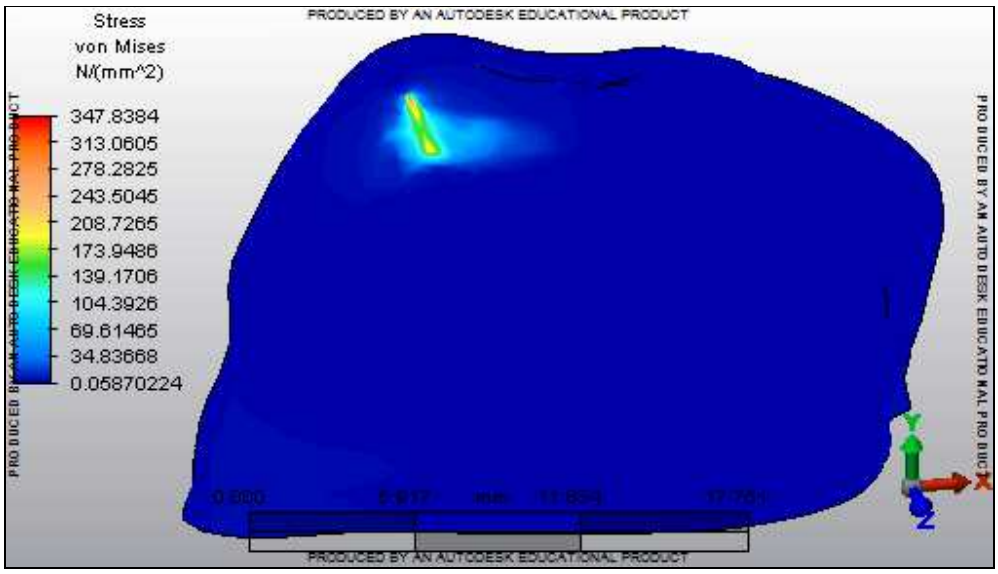

A

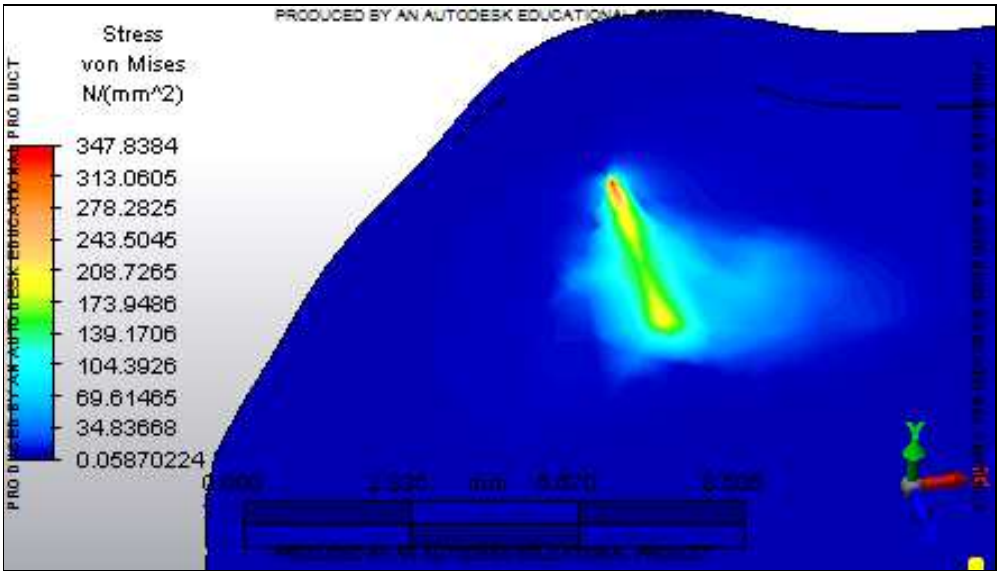

B

Figure 4-11. Maximum Von Mises Stress; A: Whole Implant, B: Close-Up View.

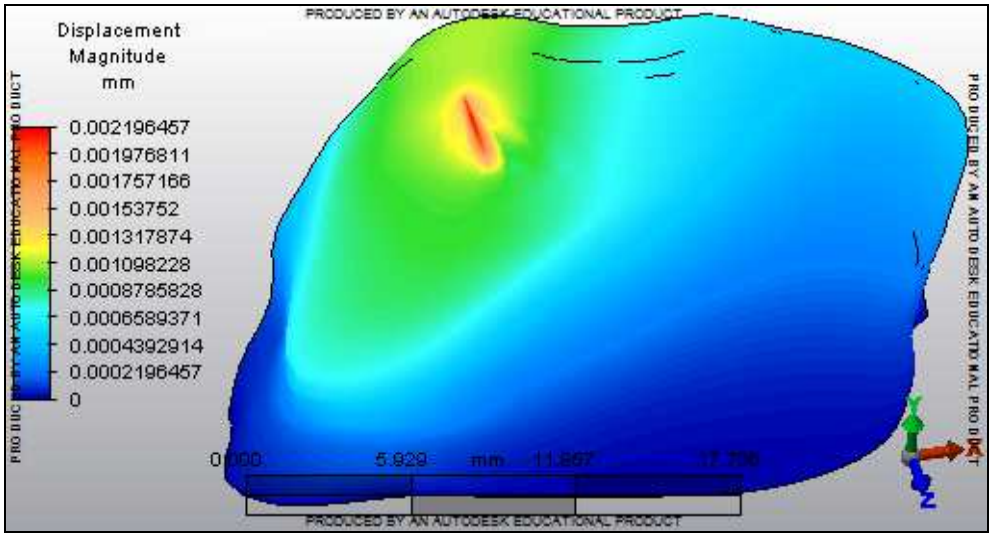

Figure 4-12. Displacement Magnitude.

Table 4-5. Stress and Displacement of the Implant.

Max. Von-Mises Stress (MPa)	Max. Von-Mises Strain	Max. Magnitude Displacement (mm)
347.83	0.009	0.002

4.4 Machining Experiments for the Implant

In this section, the optimized machining conditions determined in Section 4.2 are verified by completing the roughing cycle for the implant for two different chip loads; 0.10 mm/tooth and 0.05 mm/tooth.

4.4.1 Rough Machining of the Implant

The tool that was used in the roughing experiments has the same diameter and flute configuration as one used in Section 4.2. However, the roughing tool here has 20 mm neck length, as shown in Figure 4-13, for better access to the implant. The previous tool had a neck length of 12 mm. There will be two implants machined to determine whether the 0.05 mm/tooth or 0.10 mm/tooth chip load provides better surface integrity. The cutting speed of 30 m/min, tool engagement of 120°, and depth of cut of 3 mm will remain the same during the rough machining of the two implants.

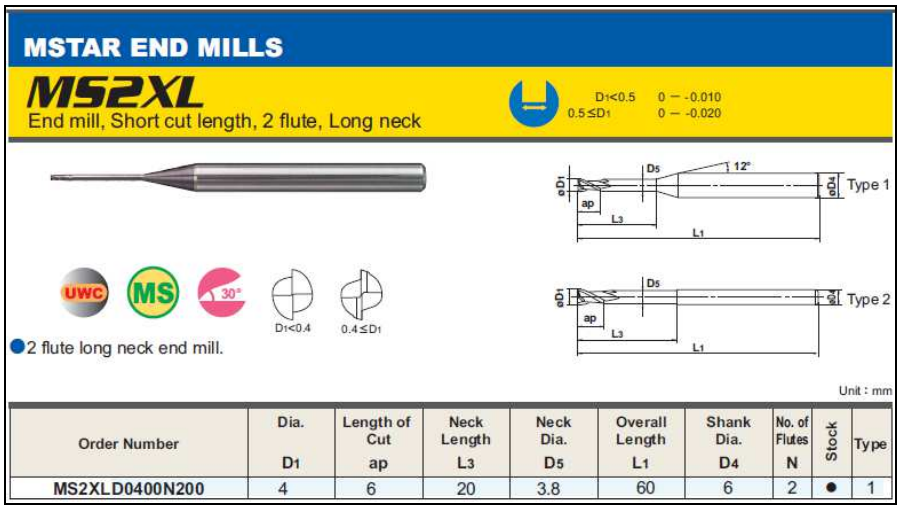

Order Number	Dia. D1	Length of Cut ap	Neck Length L3	Neck Dia. D5	Overall Length L1	Shank Dia. D4	No. of Flutes N	Stock	Type
MS2XLD0400N200	4	6	20	3.8	60	6	2	●	1

Figure 4-13. Mitsubishi tool selected for Roughing Stage of Tibia Plateau Implant.

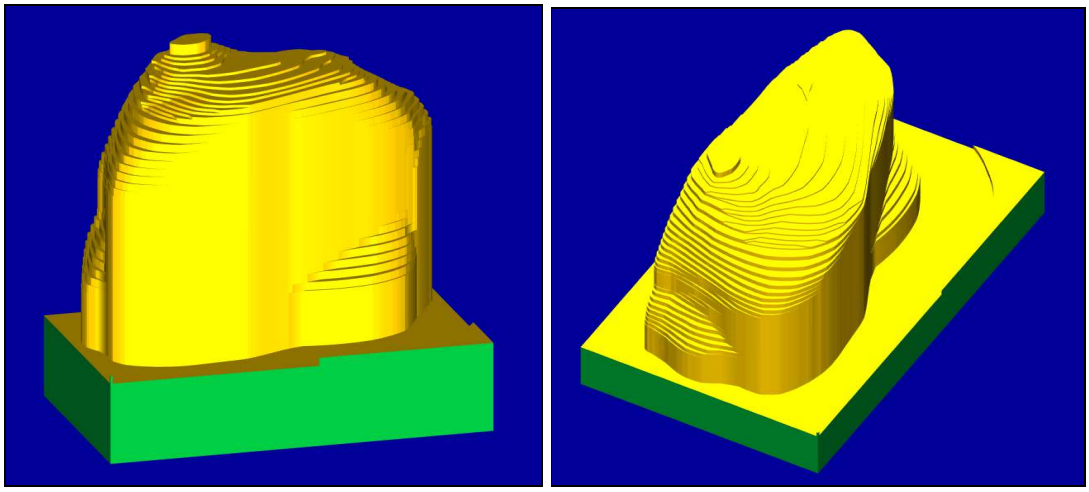

Figure 4-14. Master CAM verified images of the roughing stage of Tibia Plateau Implant.

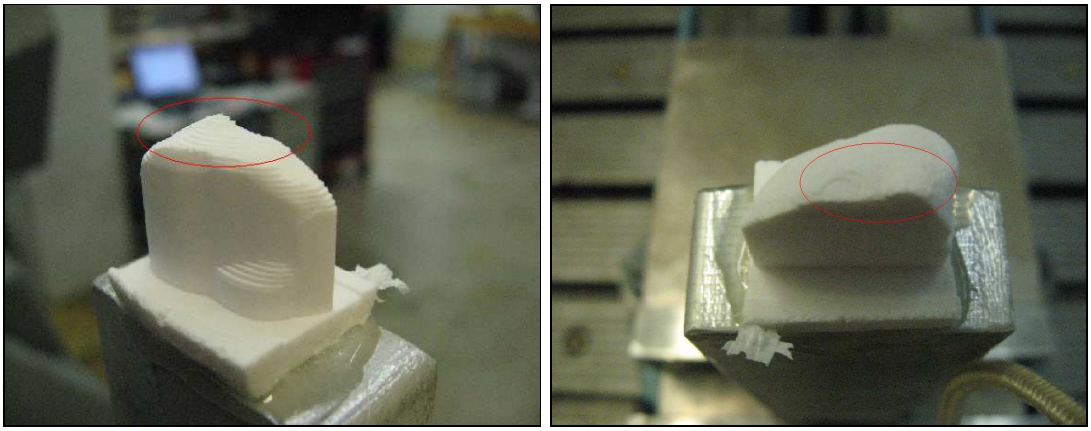

Figure 4-15. Machined Tibia Plateau Implant at 0.05mm/tooth Chip Load.

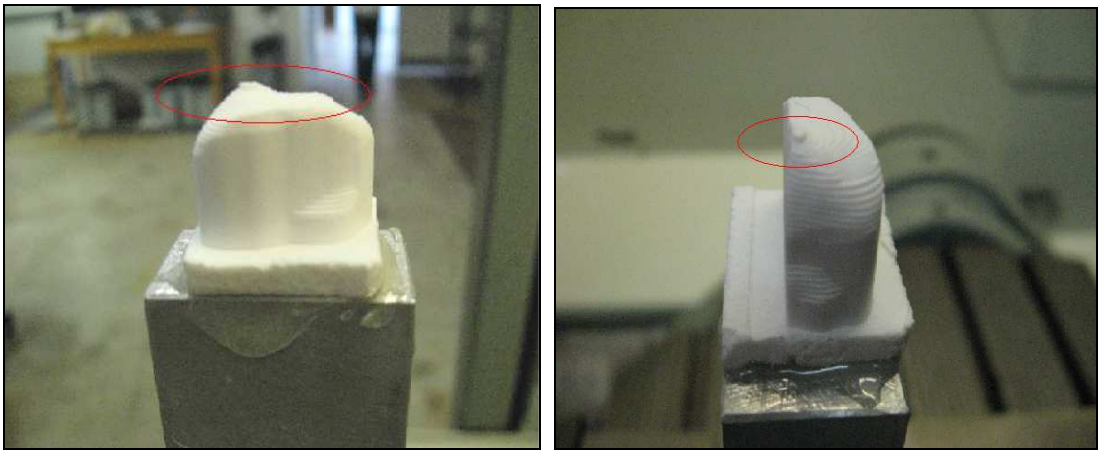

Figure 4-16. Machined Tibia Plateau Implant at 0.1 mm/tooth Chip Load.

Once the toolpath is programmed in MasterCAM X3 (.MCX) and the parameters are placed in their category, the NC (Numerical Code) file is generated which is fed to the CNC controller.

Figure 4-14 presents a simulation of roughing operation in MasterCAM X3. The simulation shows what the implant should look like after roughing. Figures 4-15 and 4-16 show the roughed implants produced with 0.05 mm/tooth and 0.10 mm/tooth chip loads, respectively.

The top of each implant, where chipping is most likely to occur, has been circled with red color in each figure. Both roughed parts seem to have excellent surface integrity. However, slightly better quality was observed in the implant machined with the higher chip load, which is difficult to explain for the time being and could just be a random effect that needs further investigation. Overall, by applying the optimized machining conditions including 0.10 mm/tooth chip load, a material removal rate of 4,302 mm^3/min was achieved. This is noted to be over 14 times higher than the material removal rate of 300 mm^3/min, which was achieved for rough machining CPP in the earlier work preceding this thesis [16][8].

4.4.2 Machining Cycle Time Comparison in the Roughing Stage

Shorter machining cycle time indicates better productivity. Using the machining parameters in the earlier work [8] causes the roughing process to take approximately 159 minutes. This can be very adverse when the time cost per implant is considered. Table 4-6 presents the machining parameters and cycle times achieved in the earlier work for machining the CPP implant, and the results obtained in this thesis. The cycle times were computed using MasterCAM simulations.

As can be seen, by implementing the machining conditions optimized in this thesis, the cycle times have been decreased by approximately by eight times. Originally it took 108 minutes to complete the first roughing operation (Surface Rough Pocketing) and 51 minutes to complete the second (Surface Finish Contouring). Machining the ionic bonding polymer infiltrated CPP with the new parameters took only a total of 19 minutes to complete. This has removed 140 minutes of machining time, as shown with the bar graph in Figure 4-17.

Table 4-6: Earlier Reported and Currently Achieved Process Cycle Times.

	Earlier Work [8]	**Currently Achieved**
Material	Porous CPP	CPP+ Bonding Polymer
Cutting Tool	4 Flute, 3/16" Flat End Mill	2 Flute, 4mm Flat End Mill
Toolpath #1	Surface Rough Pocket	Surface Rough Pocket
Machining Parameters	DOC 2 mm, Exit Angle 90°, Cut Speed 22.4 m/min, Chip Load 0.0125 mm/tooth	DOC 3 mm, Exit Angle 120°, Cutting Speed 30 m/min, Chip Load 0.1 mm/tooth
Cycle Time	108 min.	**11 min.**
Toolpath #2	Surface Finish Contour	Surface Finish Contour
Machining Parameters	DOC 0.5 mm, Cutting Speed 22.4 m/min, Chip Load 0.0125 mm/tooth	DOC 0.5 mm, Cutting Speed 30 m/min, Chip Load 0.1 mm/tooth
Cycle Time	51 min.	**8 min.**
Total Cycle Time	159 min.	**19 min.**

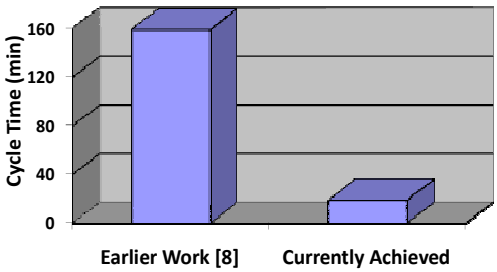

Figure 4-17. Bar Graph Comparing Earlier and Currently Achieved Roughing Cycle Times.

4.5 Conclusions

In the beginning of this chapter, experiments were developed to refine the machining conditions to optimize the roughing process for surface integrity. It was determined that a certain depth of porosity loss, typically less than 1.3 mm, could be tolerated due to the use of latter finishing operations which would ultimately trim away the smudged later. With these kept in mind, for CPP infiltrated with the ionic bonding polymer, the following conditions were determined to be highly suitable for achieving both high productivity as well as excellent surface integrity:

- 2 fluted 4 mm diameter flat end mill
- 30 m/min cutting speed
- ¾ immersion up-milling with 0.1 mm chip load and 3 mm depth of cut

These conditions produced a material removal rate of 4,302 mm^3/min, which was 14 times higher than the material removal rate achieved for machining pure CPP in earlier studies.

The cutting force coefficients for polymer infiltrated CPP were identified for the first time in machining literature, which have been summarized in Table 4.2. The constructed machining model was highly successful in predicting the cutting forces, and therefore can be used in process planning and optimization in the production of tissue engineered implant constructs out of CPP.

The Finite Element analyses predicted that the implant would not chip or break during the roughing operation, as validated experimentally. Also, the stress levels around the vicinity of the tool contact were in agreement with the experimental trends observed for un-infiltrated and infiltrated CPP samples.

Finally, the optimized machining conditions have been validated in rough machining of a tibial plateau implant, where the roughing cycle time was reduced from 159 min to 19 min, effectively achieving a productivity improvement of 8 times over the earlier work done in this area.

CHAPTER 5
Conclusion

This thesis has investigated the improvement of machining productivity for CPP implants. Since the majority of the time in machining is dedicated to the roughing operation, this task was chosen as the target for achieving the maximum cycle time reduction. Using Taguchi's method, the minimum number of experiments were designed that allowed the major factors that influence the CPP machining operation to be investigated. These factors were: material composition, cutting speed, chip load, depth of cut, and tool engagement. It was determined that up-milling CPP stock that is infiltrated with an ionic-bonding polymer, using a 2-fluted 4 mm diameter end mill at 30 m/min cutting speed, under ¾ immersion, 0.1 mm chip load, and 3 mm depth of cut provide a material removal rate of 4,302 mm^3/min, which is 14 times higher than the roughing productivity which was achieved in the earlier study. Under these conditions, as excellent surface and feature integrity could be consistently obtained. Although there was some loss of porosity compared to machining pure CPP, this was deemed acceptable for the implant's clinical function by the biomedical researchers at the University of Toronto. Furthermore, the depth of the smudged layer was only around 50 microns, and would typically be removed during consecutive semi- or final-finishing operations.

A cutting force model for this material was constructed, by identifying the cutting force coefficients for the first time and validating the experimentally measured force profiles with simulations. This model can be used for process planning and optimization in the production of tissue engineered implants.

Finite Element analyses were conducted, which predicted that the implant would not chip or break during the roughing operation due to fixturing and cutting force overload, as was verified experimentally. The stress levels around the vicinity of the tool contact area also explained why pure CPP broke off or chipped more easily, while the stock of CPP infiltrated with the ionic bonding polymer did not.

Finally, the results of these studies were incorporated into planning the machining operation of a tibial plateau implant. This allowed the roughing cycle time to be reduced from 159 min to 19 min, effectively achieving a productivity improvement of 8 times over the earlier work done in this area.

References

[1] Alintas, Y., (2000). *Manufacturing Automation: Principles of Metal Cutting and Machine Tool Control. Cambridge University Press.* ISBN 0521659736.

[2] Montgomery, D. C., Runger, G., Hubele, N. F. (2011). *Engineering Statistics: 5th Edition. Hoboken, NJ: John Wiley & Sons.* ISBN 139780470631478.

[3] Phadke, M. S., (1989). *Quality Engineering Using Robust Design. P T R Prentice-Hall Inc*. 0137451679.

[4] Griffith, E. J., (1995). *Phosphate Fibers. Plenum Press.* ISBN 030645145X.

[5] O'Shea, T. M., Miao, X., (2008). "Bilayered Scaffolds for Osteochondral Tissue Engineering", *Tissue Eng.,* Vol. 14 No.4, pp. 447-460.

[6] Guo, Y. B., Salahshoor, M., (2010). "Process Mechanics and Surface Integrity by High-Speed Dry Milling of Biodegradable Magnesium-Calcium Implant Alloys", *Annals of the CIRP*, 59:151-154.

[7] Kasuga, T., Nogami, M., Niinomi, M., (2003). "Novel Machinable Calcium Phosphate Glass-Ceramics for Biomedical Use", *Mater. Sci. Forum*, Vols. 426-432, pp. 3183-3188.

[8] Rouzrokh, A., Wei, C. Y. H., Erkorkmaz, K., Pilliar, R. M., (2010). "Machining Porous Calcium Polyphosphate Implants for Tissue Engineering Applications", *Int. J. of Autom. Tech.*, Vol.4 No.3, pp. 291-301.

[9] Chelulea, K. L., Cooleb, T. J., Cheshire, D. G., (2002). "An Investigation into the Machinability of Hydroxyapatite for Bone Restoration Implants", *J. Materials Processing Technology*, 135-2,3, pp. 242-246.

[10] Chen, S., Head, D., Effgen, M., Jawahir, I. S., (2005). "An Investigation of Sustained Machining Performance for Controlled Surface Quality Requirements in Porous Tungsten", *IEEE*, Vol. 52 No.5, pp. 903-908.

[11] Ding, Y. L., Chen, Y. W., Qin, Y. J., Shi, G. Q. S., Yu, X. X., Wan, C. X., (2008). "Effect of polymerization degree of Calcium Polyphosphate on its Microstructure and In Vitro Degradation Performance", *J. Mater Sci: Mater Med.*, 19:1291-1295.

[12] Shanjani, Y., De Croos, J. N. A., Pilliar, R. M., Kandel, R. A., Toyserkani, E., (2010). "Solid Freeform Fabrication and Characterization of Porous Calcium Polyphosphate Structures for Tissue Engineering Purposes", *Journal of Biomedical Materials*, Vol. 93B, ISSUE 2, pp. 510-519.

[13] Grynpas, M. D., Pilliar, R. M., Kandel, R. A., Renlund, R., Filiaggi, M. J., Dumitriu, M., (2001). “Porous calcium polyphosphate scaffolds for bone substitute applications in vivo studies”, *Biomater*., Vol. 23 No.9, pp. 2063-2070.

[14] Pilliar, R. M., Filiaggi, M. J., Wells, J. D., Grynpas, M. D., Kandel, R. A., (2001). “Porous calcium polyphosphate scaffolds for bone substitute applications - in vitro characterization”, *Biomater*., Vol. 22 No.9, pp. 963-972.

[15] Wei C., (2007), “Rapid Fabrication Techniques for Anatomically-Shaped Calcium Polyphosphate Substrates for Implants to Repair Osteochondral Focal Defects”, Master’s Thesis, University of Waterloo, 200 University Ave. West, Waterloo, Ontario Canada.

[16] Rouzrokh A., (2008), “Shaping Biodegradable Bone Implants Using Computer Numerically Controlled (CNC) Multi-Axis Machining”, Master’s Thesis, University of Waterloo, 200 University Ave. West, Waterloo, Ontario Canada.

[17] 1048e015fa8e70557c658acaae053cbf_LARGE.png grin.com, 2007.

[18] Filiaggi M, Pilliar R.M., and Hong J., (2001), “On the Sintering Characteristics of Calcium Polyphosphates”, *Key Engineering Materials*, 192-195, pp. 171-174.

[19] Bammann D.J., Chiesa M.L., Johnson G.C., (1996), “Modeling Large Deformation and Failure in Manufacturing Processes, Theoretical Applied Mechanics”, Elsevier Science B.V.

[20] Liu C.R., Mittal S., (1995), “Single-step Superfinishing Using Hard Machining Resulting in Superior Surface Integrity”, *J. Manufact. Syst*., vol.14, no.2, pp. 129-133.

[21] Yang L., Wang J., Hong J., Santerre J.P., Pilliar R.M., (2003) “Synthesis and characterization of a novel polymer-ceramic system for biodegradable composite applications”. *J Biomed Mater Res*, 66A:622-632.

[22] Kandel R. A., Grynpas M. D., Pilliar R. M., Lee J., Waldman S. D., Zalzal P., Hurtig M., (2006) “Repair of Osteochondral Defects with Biphasic Cartilage-Calcium Polyphosphate Constructs In a Sheep Model”, *Biomaterials*, 27, pp. 4120-4131.

[23] Gan L., Tse C., Pilliar R. M., Kandel R. A., (2007) “Low-Power Laser Simulation of Tissue Engineered Cartilage Tissue Formed on a Porous Calcium Polyphosphate Scaffold”, *Lasers Surg Med*., 39, pp. 286-293.

[24] Allan K., Pilliar R. M., Wang J., Grynpas M. D., Kandel R. A., (2007) “Formation of Biphasic Constructs Containing Cartilage with a Calcified Zone Interface”, *Tissue Engineering*, 13, pp. 167-77.

[25] Kelly J. R., Antonucci J. M., (1997) “Processing and properties of interpenetrating phase composites”, *Polymer Preprints*, 38, pp. 125–126.

[26] Clark P. R., (1992) “Interpenetrating phase composite”, *J Am Ceram Soc*,75, pp. 739 – 759.

[27] Cipera E. D., (1998) “Development of a Novel Interpenetrating Phase Composite”, Master’s Thesis, University of Toronto, Toronto, Ontario Canada.

[28] Wang Q., Wang Q., Zhang X., Yu X., Wan C., (2010) “The Effect of Sintering Temperature on the Structure and Degradability of Strontium-Doped Calcium Polyphosphate Bioceramics”, *Ceramics– Silikáty* 54, (2) 97-102.

[29] Shin, H., Ruhe, P.Q., Mikos, A.G., and Jansen, J.A., (2003), “In vivo bone and soft tissue response to injectable, biodegradable oligo(poly(ethylene glycol) fumarate) hydrogels”, *Biomater.*, Vol. 24, pp. 3201–3211.

[30] Ozel, T., Altan, T., (2000) “Process simulation using finite element method — prediction of cutting forces, tool stresses and temperatures in highspeed flat end milling”, *International Journal of Machine Tools & Manufacture.*, Vol. 40, pp. 713–738.

[31] Shi, D., (2004). *Biomaterials and Tissue Engineering. Springer Berlin Heidelberg New York*. ISBN 3540222030.

Appendices

Appendix A

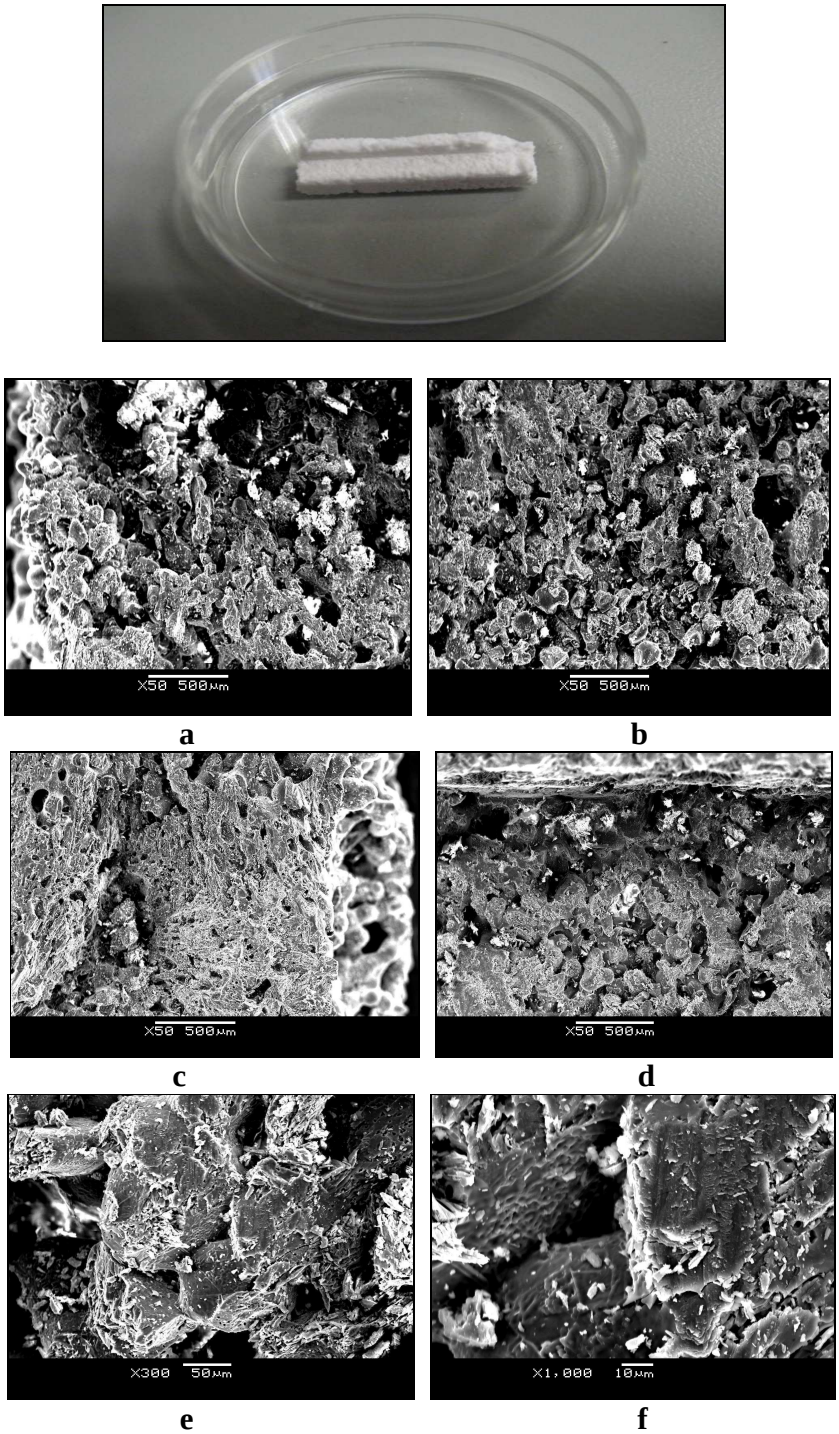

Figure A-1: Run 2 CPP Non-Infiltrated, Depth of Cut: 2mm, Chip Load: 0.1mm/tooth, Cut Speed: 20m/min. (From top left to bottom right. **a.** Entrance of the cutpass, **b.** middle of the cutpass, **c.** exit of the cutpass, **d.** inner edge of the cutpass, **e & f.** higher magnification of middle cutpass)

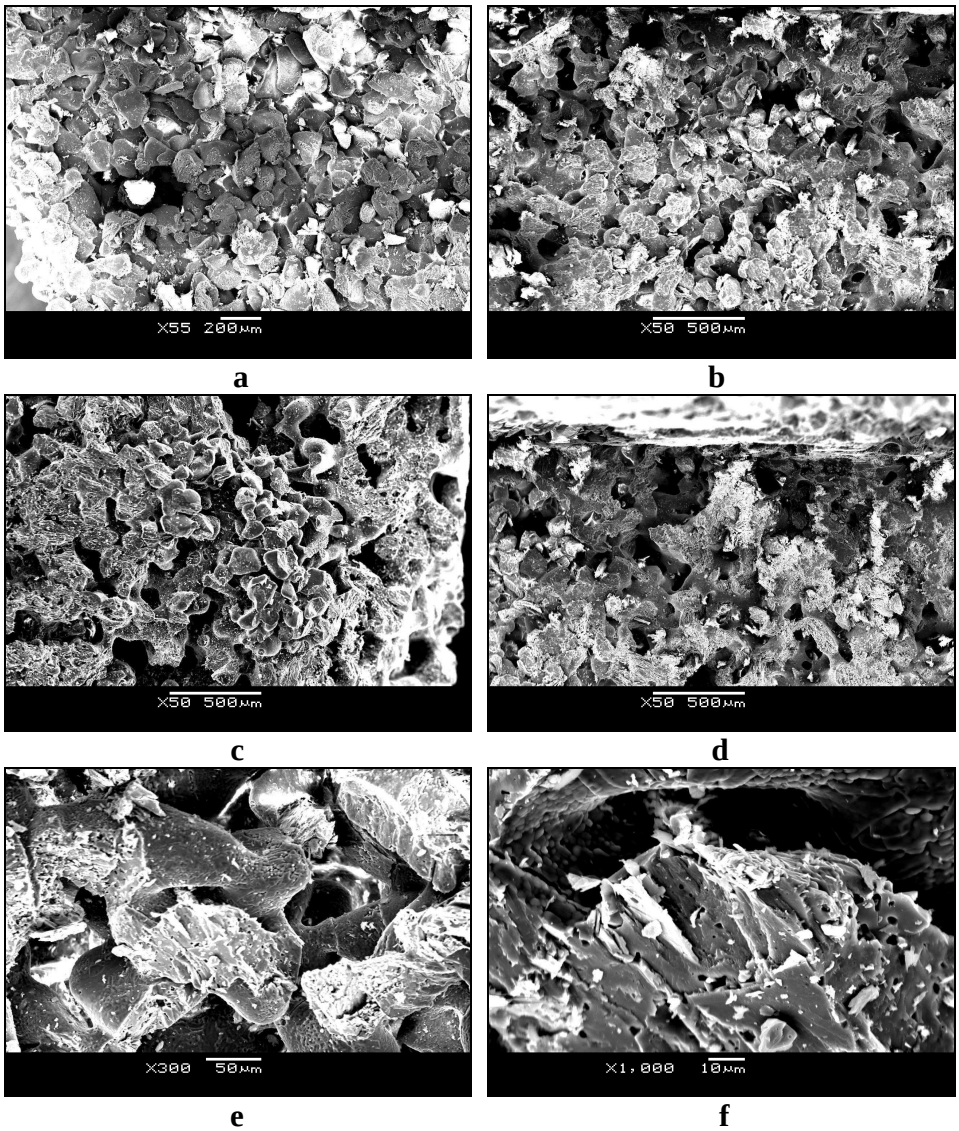

Figure A-2: Run 3 CPP Non-Infiltrated, Depth of Cut: 3mm, Chip Load: 0.15mm/tooth, Cut Speed: 30m/min. (From top left to bottom right. **a.** Entrance of the cutpass, **b.** middle of the cutpass, **c.** exit of the cutpass, **d.** inner edge of the cutpass, **e & f.** higher magnification of middle cutpass)

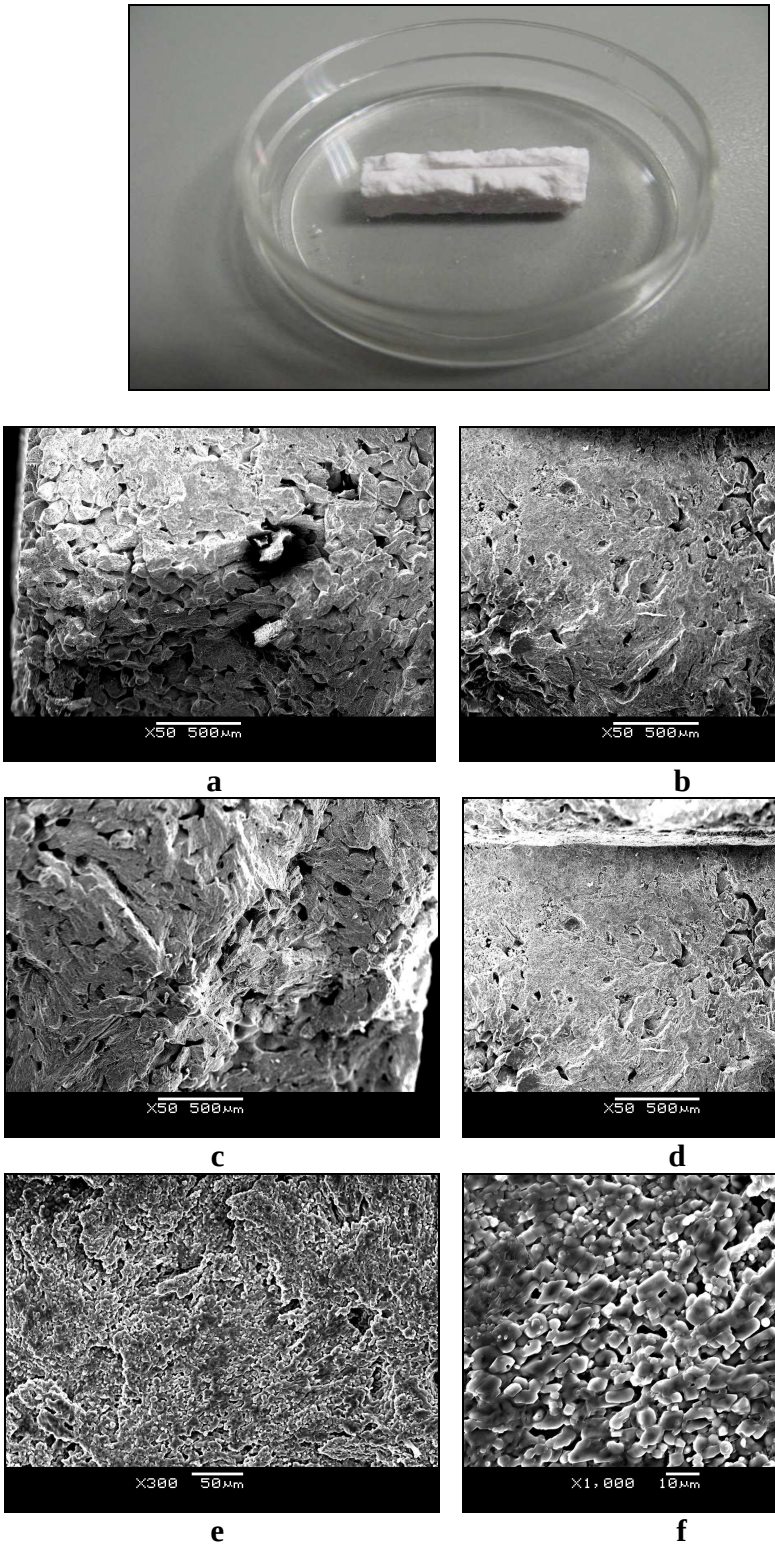

Figure A-3: Run 4 CPP Infiltrated Non-Bond, Depth of Cut: 1mm, Chip Load: 0.15mm/tooth, CutSpeed: 20m/min. (From top left to bottom right. **a.** Entrance of the cutpass, **b.** middle of the cutpass, **c.** exit of the cutpass, **d.** inner edge of the cutpass, **e & f.** higher magnification of middle cutpass)

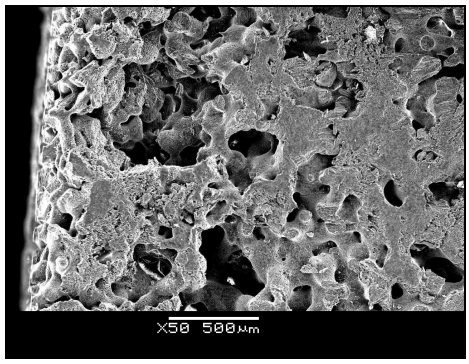

a

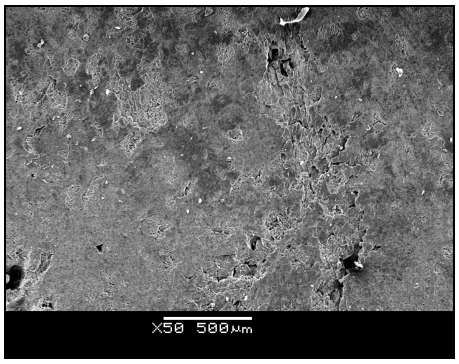

b

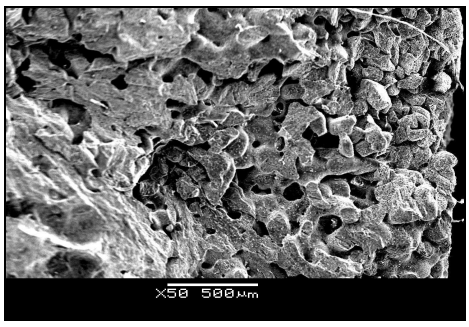

c

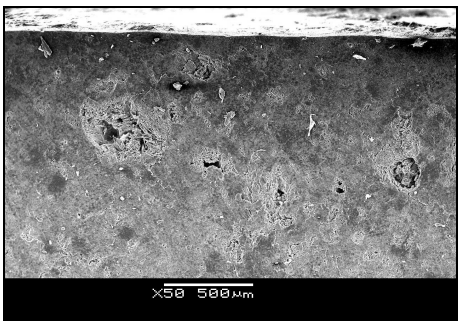

d

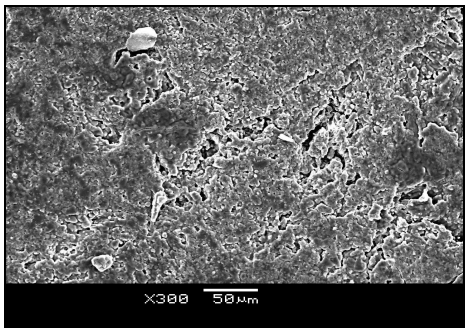

e

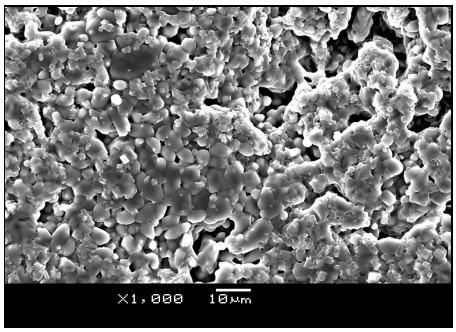

f

Figure A-4: Run 5 CPP Infiltrated Non-Bond, Depth of Cut: 2mm, Chip Load: 0.05mm/tooth, CutSpeed: 30m/min. (From top left to bottom right. **a.** Entrance of the cutpass, **b.** middle of the cutpass, **c.** exit of the cutpass, **d.** inner edge of the cutpass, **e & f.** higher magnification of middle cutpass)

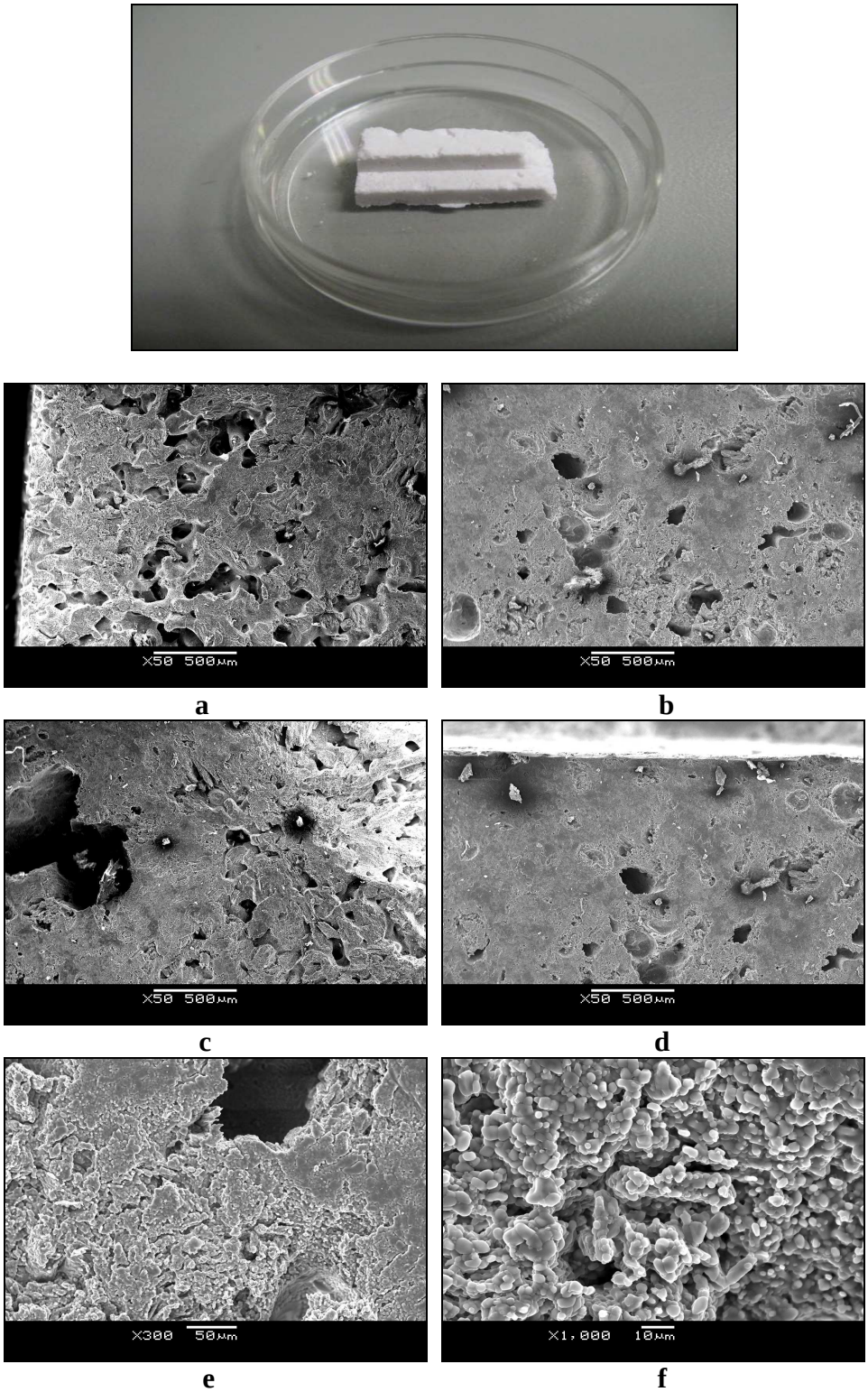

Figure A-5: Run 6 CPP Infiltrated Non-Bond, Depth of Cut: 3mm, Chip Load: 0.1mm/tooth, Cut Speed: 10m/min. (From top left to bottom right. **a.** Entrance of the cutpass, **b.** middle of the cutpass, **c.** exit of the cutpass, **d.** inner edge of the cutpass, **e & f.** higher magnification of middle cutpass)

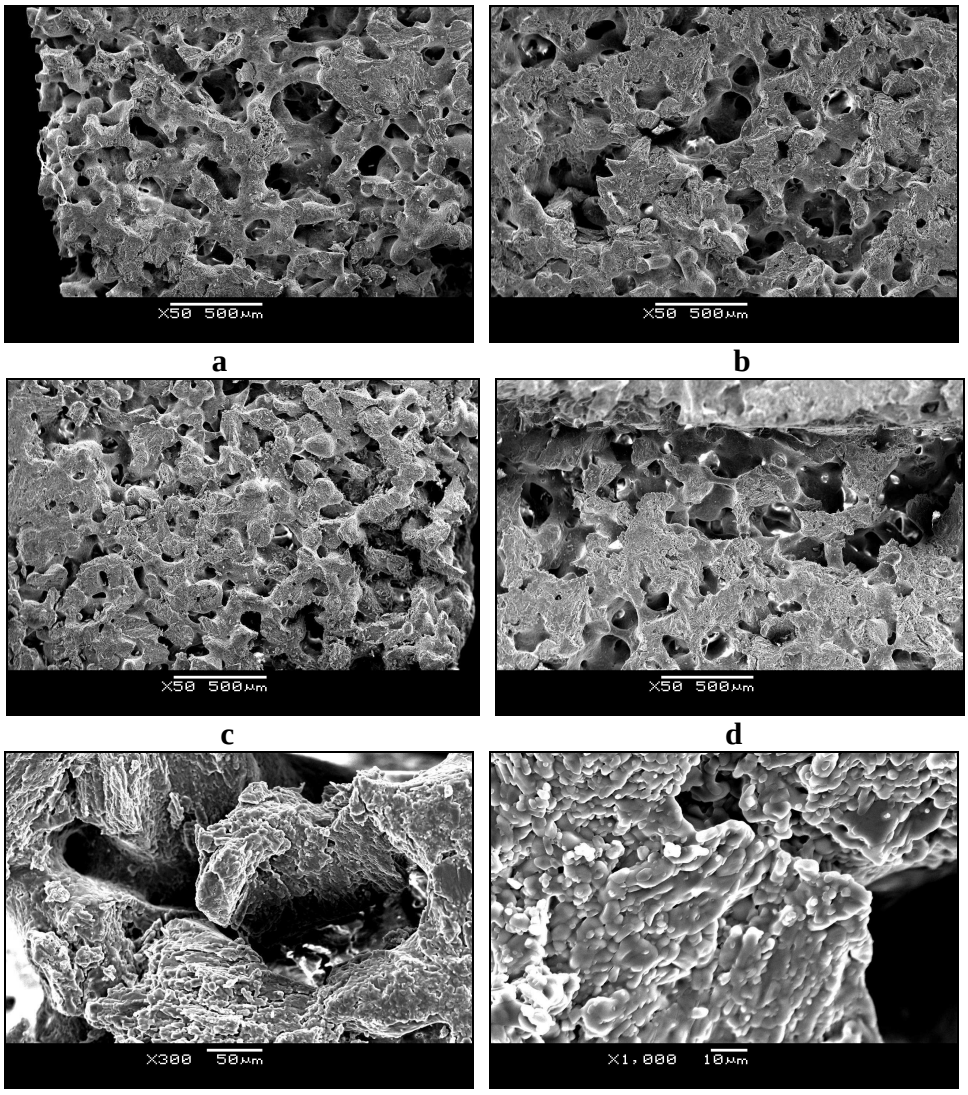

Figure A-6: Run 7 CPP Infiltrated Bond, Depth of Cut: 1mm, Chip Load: 0.1mm/tooth, Cut Speed: 30m/min. (From top left to bottom right. **a.** Entrance of the cutpass, **b.** middle of the cutpass, **c.** exit of the cutpass, **d.** inner edge of the cutpass, **e & f.** higher magnification of middle cutpass)

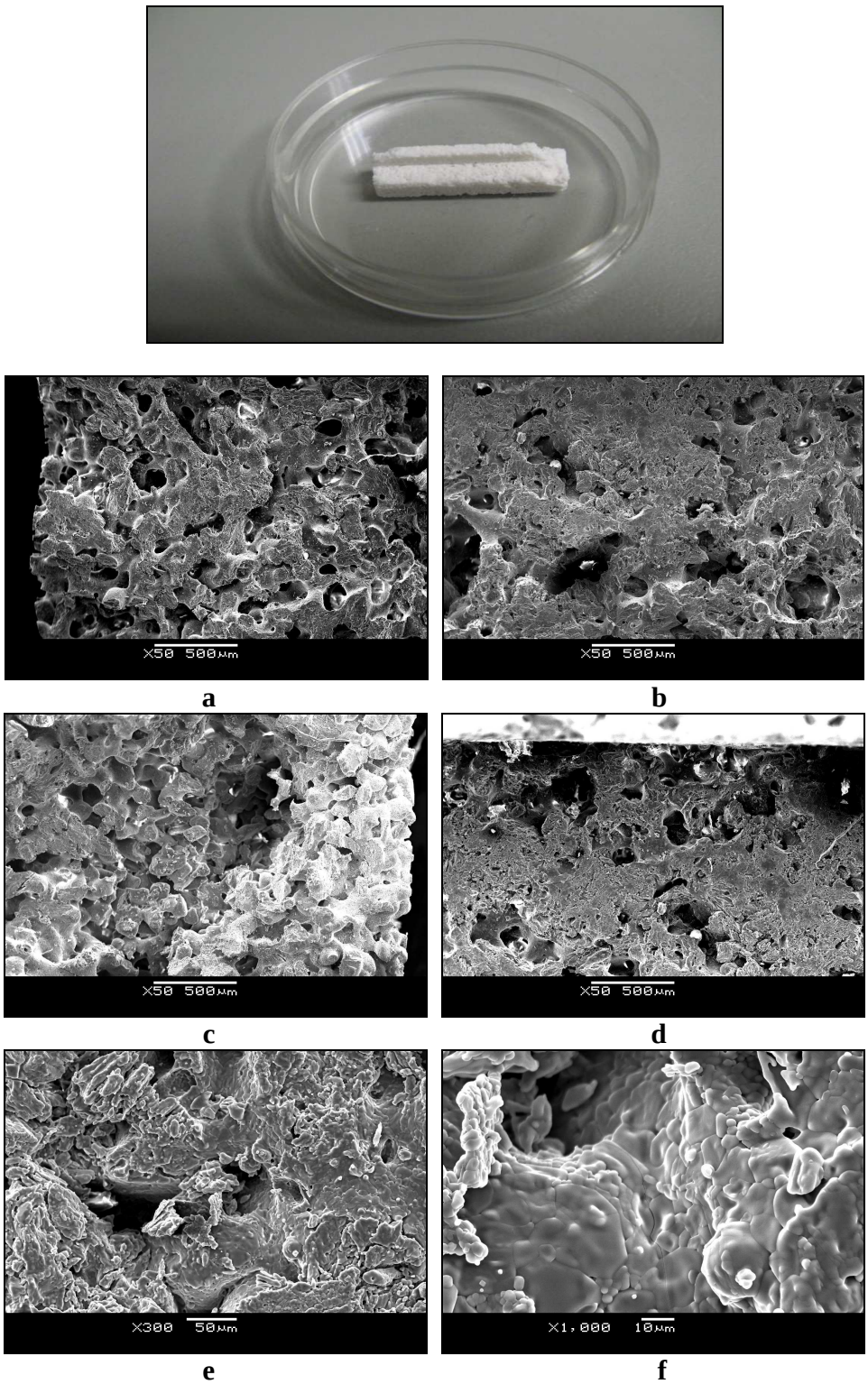

Figure A-7: Run 8 CPP Infiltrated Bond, Depth of Cut: 2mm, Chip Load: 0.15mm/tooth, Cut Speed: 10m/min. (From top left to bottom right. **a.** Entrance of the cutpass, **b.** middle of the cutpass, **c.** exit of the cutpass, **d.** inner edge of the cutpass, **e & f.** higher magnification of middle cutpass)

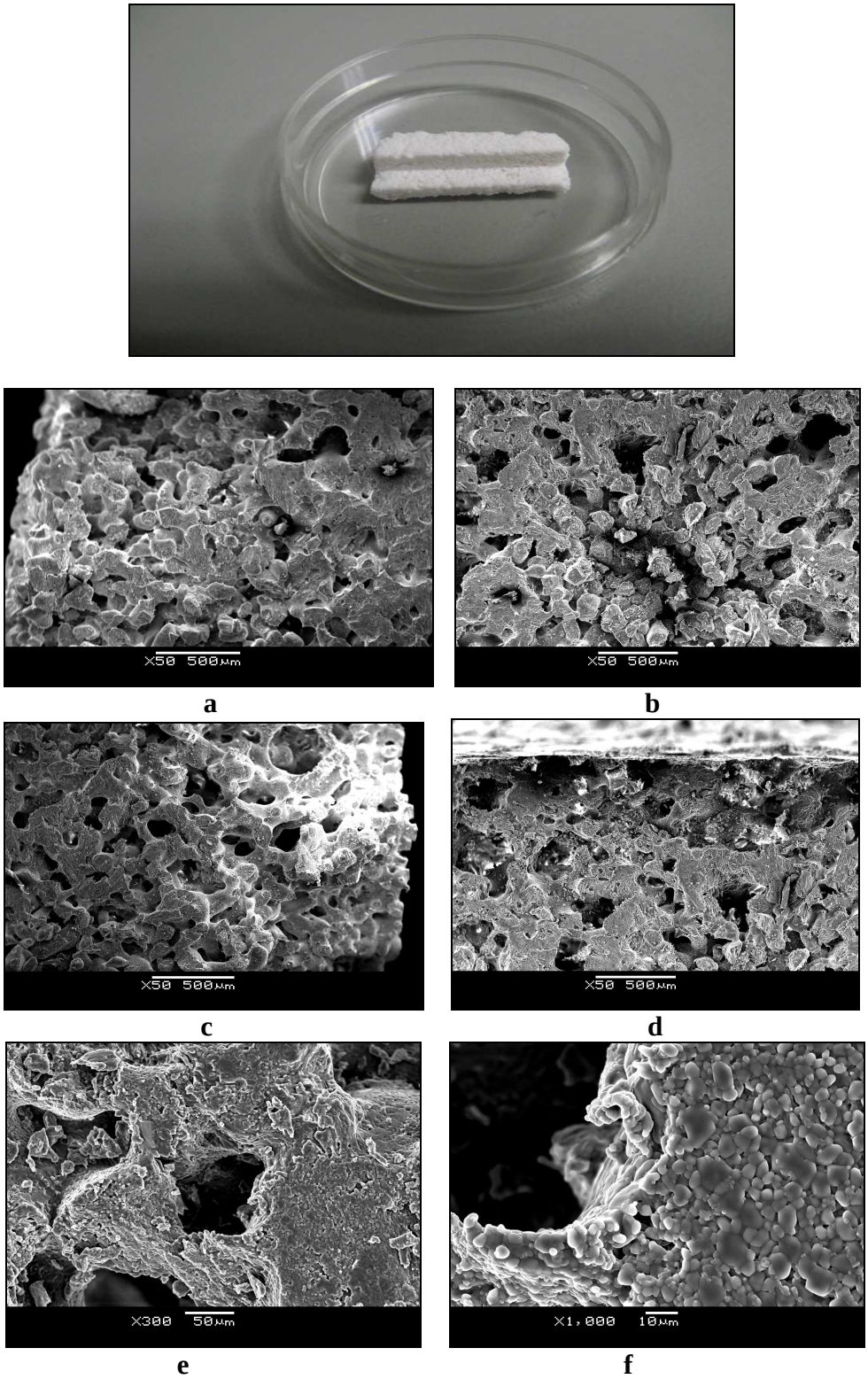

Figure A-8: Run 9 CPP Infiltrated Bond, Depth of Cut: 3mm, Chip Load: 0.05mm/tooth, Cut Speed: 20m/min. (From top left to bottom right. **a.** Entrance of the cutpass, **b.** middle of the cutpass, **c.** exit of the cutpass, **d.** inner edge of the cutpass, **e & f.** higher magnification of middle cutpass)

Appendix B

Repetition #2

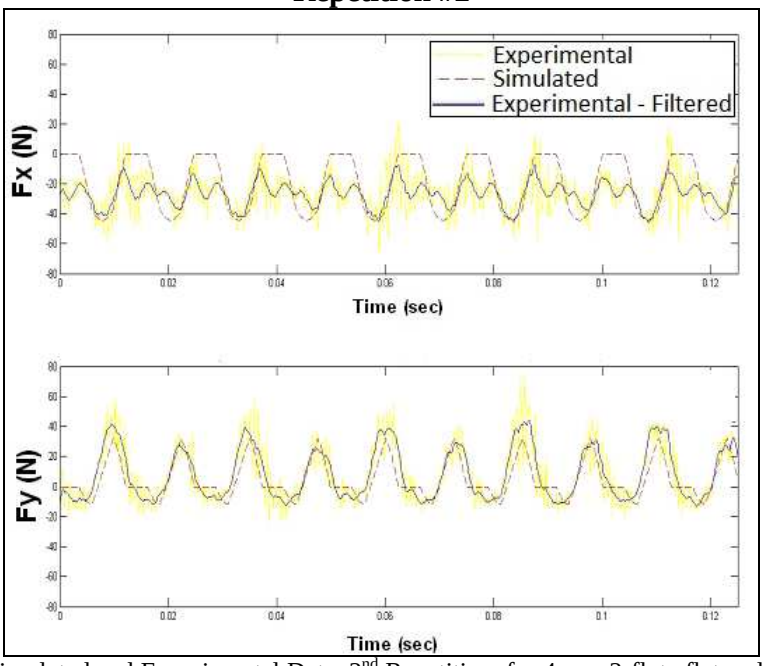

Figure B-1: Run 1 Simulated and Experimental Data, 2nd Repetition, for 4mm, 2-flute flat endmill at 30m/min Cut Speed, 0.05mm/tooth Chip Load, and 2mm DOC, Half Immersion. From top to bottom, plots refer to x and y axes respectively

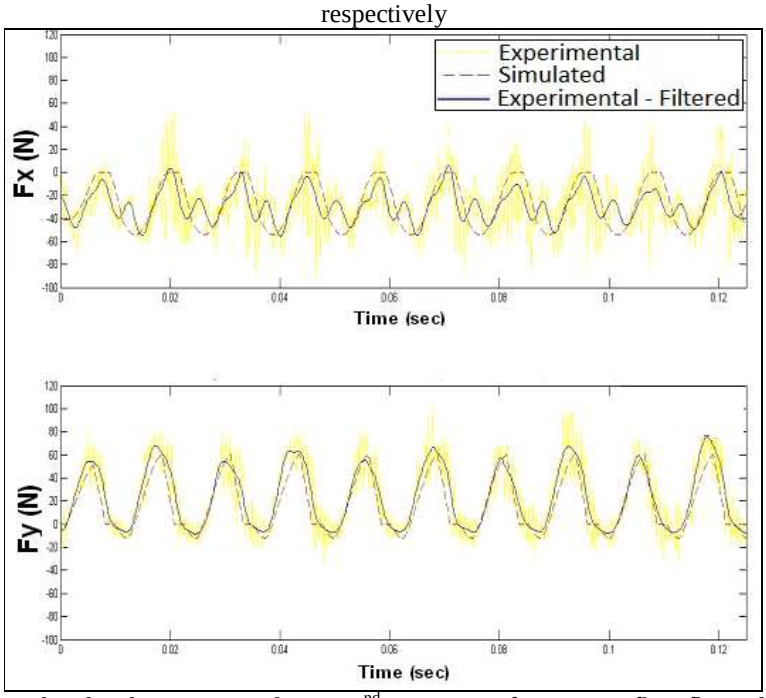

Figure B-2: Run 2 Simulated and Experimental Data, 2nd Repetition, for 4mm, 2-flute flat endmill at 30m/min Cut Speed, 0.1mm/tooth Chip Load, and 2mm DOC, 3 Quarter Immersion. From top to bottom, plots refer to x and y axes respectively

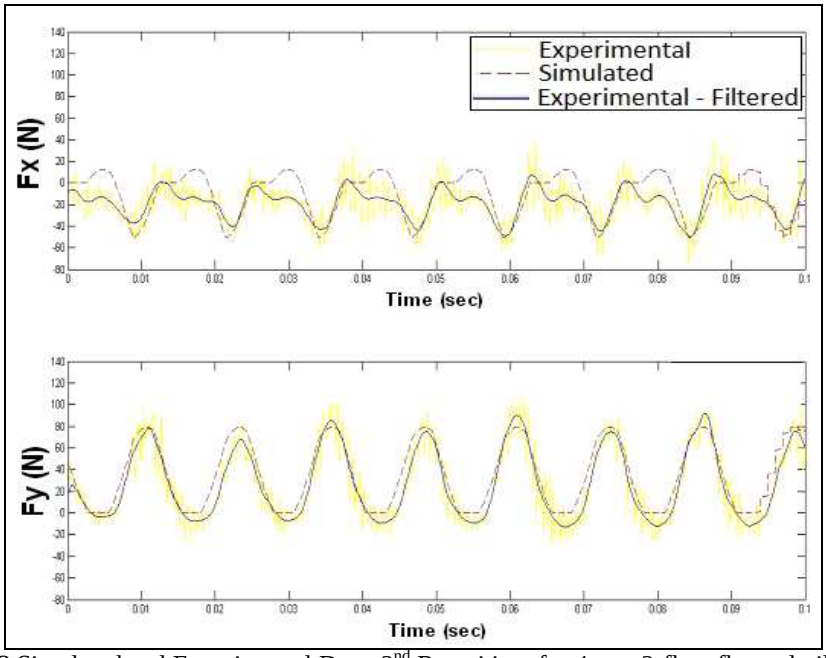

Figure B-3: Run 3 Simulated and Experimental Data, 2nd Repetition, for 4mm, 2-flute flat endmill at 30m/min Cut Speed, 0.1mm/tooth Chip Load, and 3mm DOC, Half Immersion. From top to bottom, plots refer to x and y axes respectively

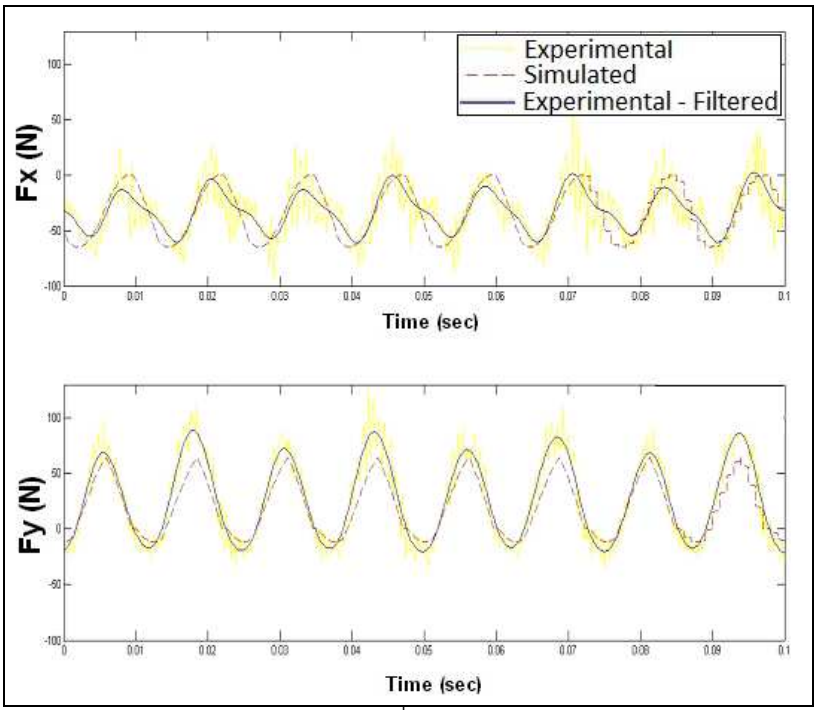

Figure B-4: Run 4 Simulated and Experimental Data, 2nd Repetition, for 4mm, 2-flute flat endmill at 30m/min Cut Speed, 0.05mm/tooth Chip Load, and 3mm DOC, 3 Quarter Immersion. From top to bottom, plots refer to x and y axes respectively

Repetition #3

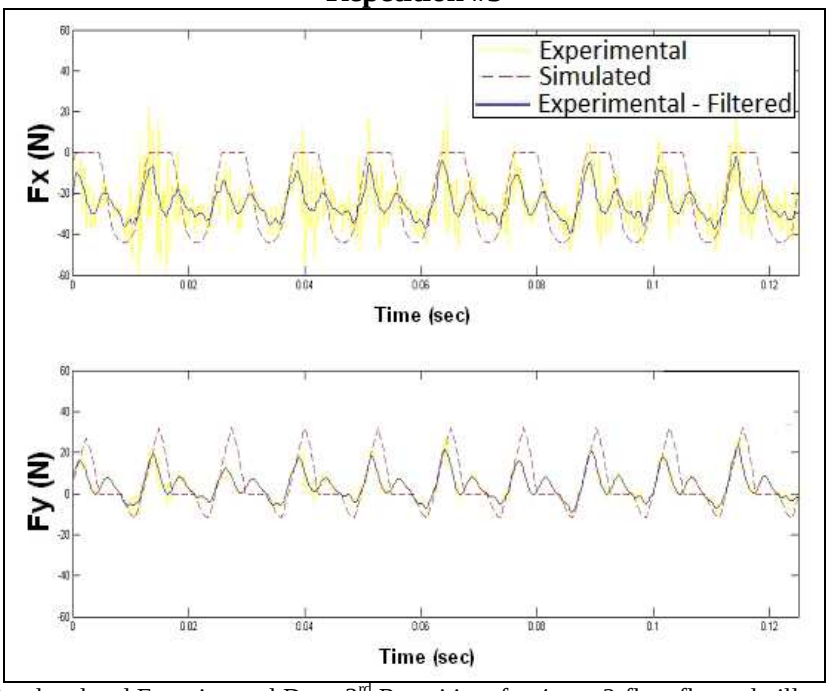

Figure B-5: Run 1 Simulated and Experimental Data, 3rd Repetition, for 4mm, 2-flute flat endmill at 30m/min Cut Speed, 0.05mm/tooth Chip Load, and 2mm DOC, Half Immersion. From top to bottom, plots refer to x and y axes respectively

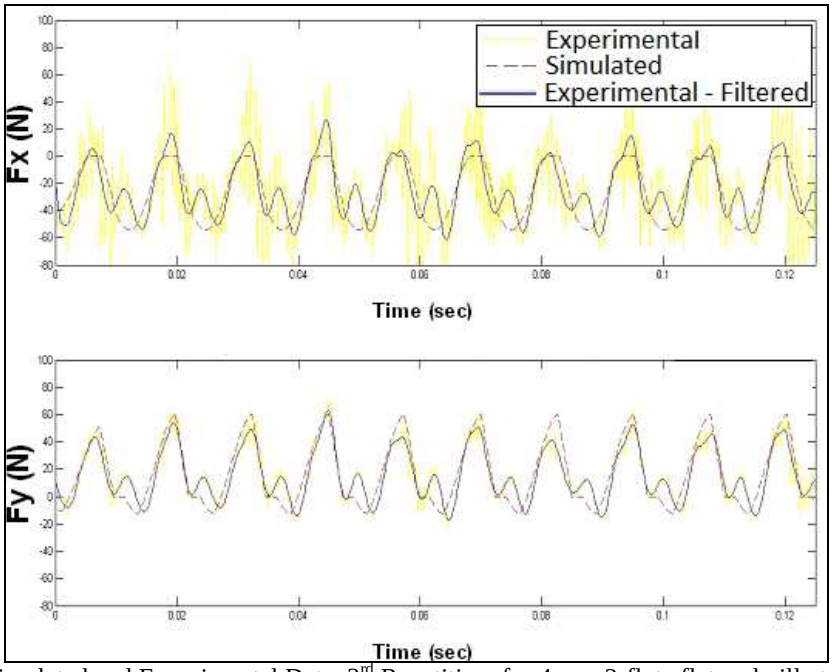

Figure B-6: Run 2 Simulated and Experimental Data, 3rd Repetition, for 4mm, 2-flute flat endmill at 30m/min Cut Speed, 0.1mm/tooth Chip Load, and 2mm DOC, 3 Quarter Immersion. From top to bottom, plots refer to x and y axes respectively

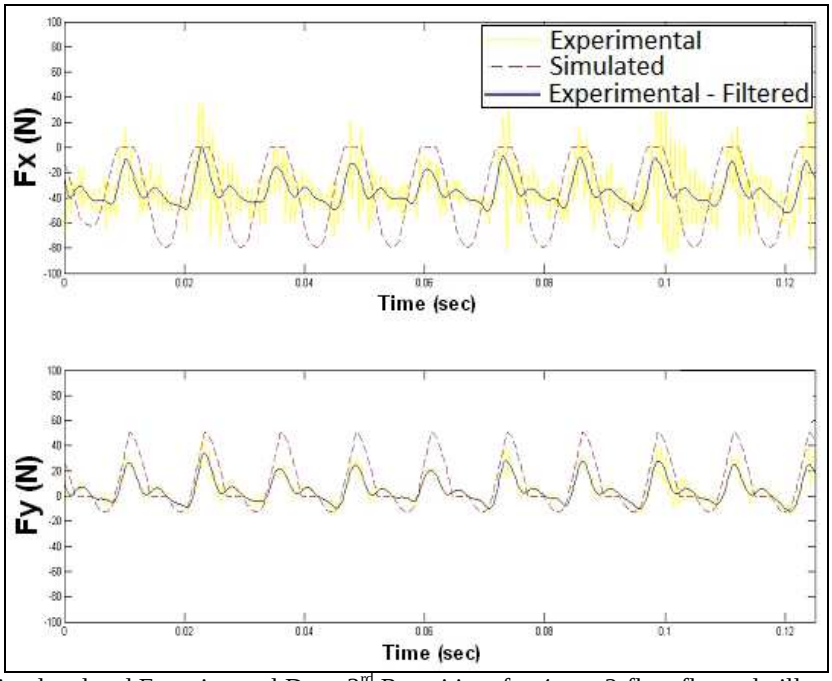

Figure B-7: Run 3 Simulated and Experimental Data, 3rd Repetition, for 4mm, 2-flute flat endmill at 30m/min Cut Speed, 0.1mm/tooth Chip Load, and 3mm DOC, Half Immersion. From top to bottom, plots refer to x and y axes respectively

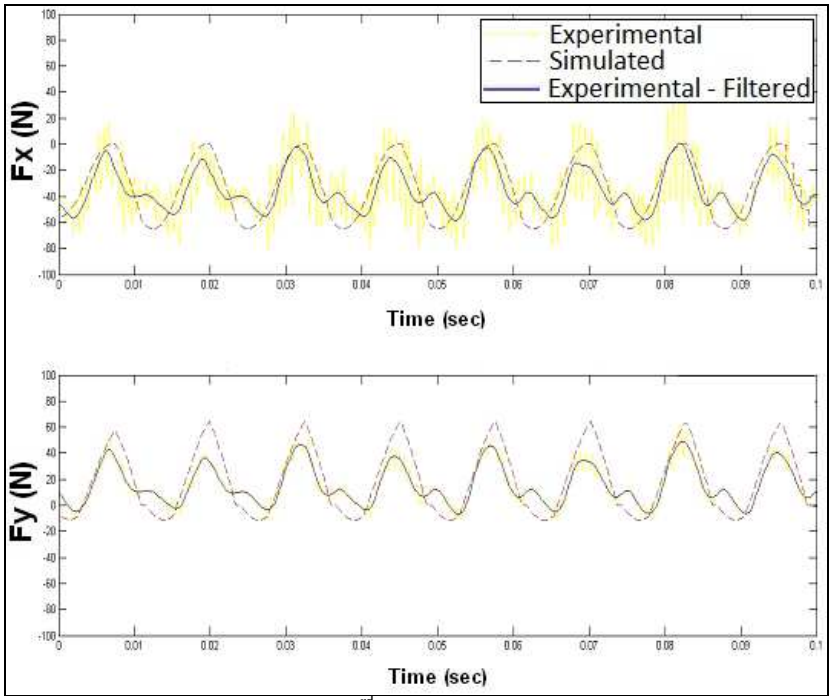

Figure B-8: Run 4 Simulated and Experimental Data, 3rd Repetition, for 4mm, 2-flute flat endmill at 30m/min Cut Speed, 0.05mm/tooth Chip Load, and 3mm DOC, 3 Quarter Immersion. From top to bottom, plots refer to x and y axes respectively

Appendix C

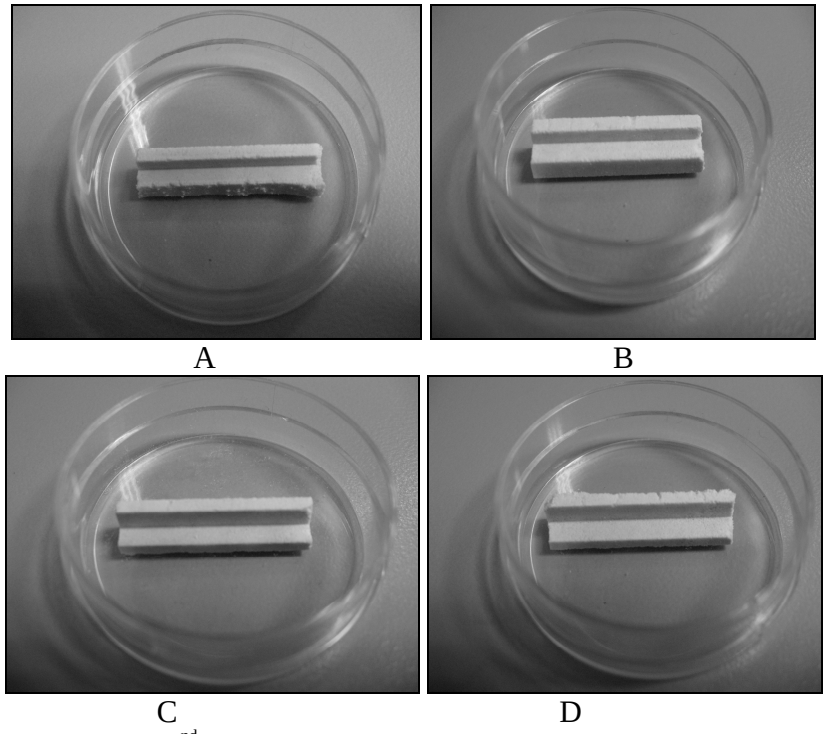

A B C D

Figure C-1: 2nd Repetition A: Run 1, B: Run 2, C: Run 3, and D: Run 4.

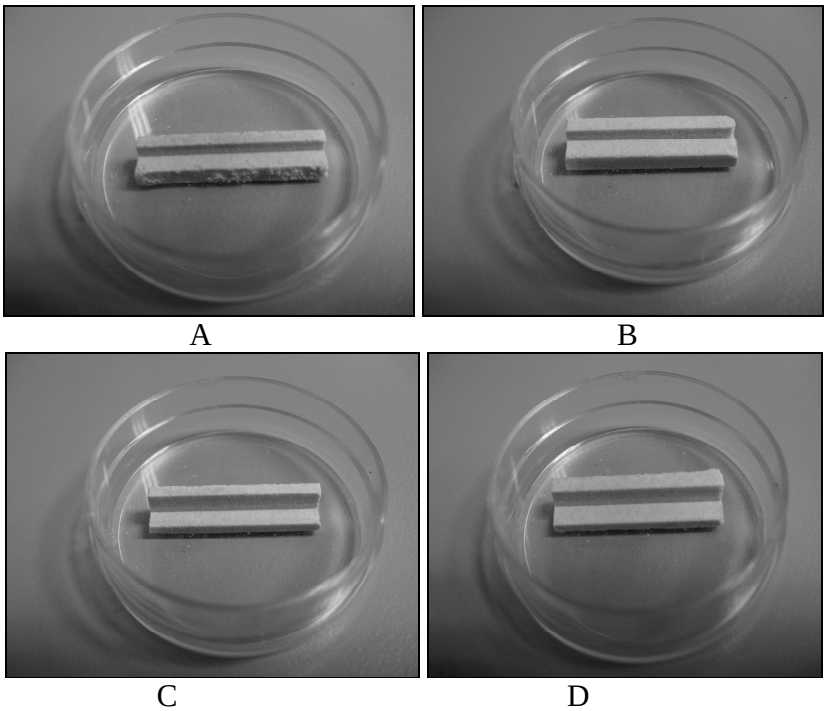

A B C D

Figure C-2: 3rd Repetition A: Run 1, B: Run 2, C: Run 3, and D: Run 4.